

# IOWA STATE UNIVERSITY

## Digital Repository

---

Retrospective Theses and Dissertations

Iowa State University Capstones, Theses and  
Dissertations

---

1973

## Delayed neutron emission from mass-separated fission products

Jay Harold Norman  
*Iowa State University*

Follow this and additional works at: <https://lib.dr.iastate.edu/rtd>



Part of the [Nuclear Engineering Commons](#), and the [Oil, Gas, and Energy Commons](#)

---

### Recommended Citation

Norman, Jay Harold, "Delayed neutron emission from mass-separated fission products " (1973). *Retrospective Theses and Dissertations*.  
S111.  
<https://lib.dr.iastate.edu/rtd/5111>

This Dissertation is brought to you for free and open access by the Iowa State University Capstones, Theses and Dissertations at Iowa State University Digital Repository. It has been accepted for inclusion in Retrospective Theses and Dissertations by an authorized administrator of Iowa State University Digital Repository. For more information, please contact [digirep@iastate.edu](mailto:digirep@iastate.edu).

## **INFORMATION TO USERS**

This material was produced from a microfilm copy of the original document. While the most advanced technological means to photograph and reproduce this document have been used, the quality is heavily dependent upon the quality of the original submitted.

The following explanation of techniques is provided to help you understand markings or patterns which may appear on this reproduction.

1. The sign or "target" for pages apparently lacking from the document photographed is "Missing Page(s)". If it was possible to obtain the missing page(s) or section, they are spliced into the film along with adjacent pages. This may have necessitated cutting thru an image and duplicating adjacent pages to insure you complete continuity.
2. When an image on the film is obliterated with a large round black mark, it is an indication that the photographer suspected that the copy may have moved during exposure and thus cause a blurred image. You will find a good image of the page in the adjacent frame.
3. When a map, drawing or chart, etc., was part of the material being photographed the photographer followed a definite method in "sectioning" the material. It is customary to begin photoing at the upper left hand corner of a large sheet and to continue photoing from left to right in equal sections with a small overlap. If necessary, sectioning is continued again — beginning below the first row and continuing on until complete.
4. The majority of users indicate that the textual content is of greatest value, however, a somewhat higher quality reproduction could be made from "photographs" if essential to the understanding of the dissertation. Silver prints of "photographs" may be ordered at additional charge by writing the Order Department, giving the catalog number, title, author and specific pages you wish reproduced.
5. PLEASE NOTE: Some pages may have indistinct print. Filmed as received.

**Xerox University Microfilms**  
300 North Zeeb Road  
Ann Arbor, Michigan 48106

74-9145

NORMAN, Jay Harold, 1937-  
DELAYED NEUTRON EMISSION FROM MASS-SEPARATED  
FISSION PRODUCTS.

Iowa State University, Ph.D., 1973  
Engineering, nuclear

University Microfilms, A XEROX Company, Ann Arbor, Michigan

Delayed neutron emission from  
mass-separated fission products

by

Jay Harold Norman

A Dissertation Submitted to the  
Graduate Faculty in Partial Fulfillment of  
The Requirements for the Degree of  
DOCTOR OF PHILOSOPHY

Department: Chemical Engineering and  
Nuclear Engineering  
Major: Nuclear Engineering

Approved:

Signature was redacted for privacy.

In Charge of Major Work

Signature was redacted for privacy.

For the Major Department

Signature was redacted for privacy.

For the Graduate College

Iowa State University  
Ames, Iowa

1973

## TABLE OF CONTENTS

	Page
I. INTRODUCTION	1
II. THEORY OF DELAYED NEUTRON EMISSION	5
III. EXPERIMENTAL METHODS	12
A. The TRISTAN Mass Separator Facility	12
B. Precursor Identification	17
C. Emission Spectra	23
D. Spectrometer Calibration Techniques	27
IV. RESULTS AND DISCUSSION	68
A. Half-life Measurements	68
B. Neutron Spectrum Measurements	75
V. CONCLUSIONS	95
VI. SUGGESTIONS FOR CONTINUING WORK	101
VII. BIBLIOGRAPHY	104
VIII. ACKNOWLEDGEMENTS	107
IX. APPENDIX A: ACTIVITY SEPARATION TECHNIQUES USING A MOVING TAPE COLLECTOR	109
A. Introduction	109
B. Definition of Data Cycles	109
C. Summary of ISOBAR Modifications	116
D. ISOBAR Calculation for Mass 93	118
X. APPENDIX B: EXPERIMENTAL EQUIPMENT USED	122
A. Half-life Measurements	122
B. $^3\text{He}$ Proportional Counter	123
C. $^3\text{He}$ Ionization Chamber	124

## LIST OF ILLUSTRATIONS

	Page
Figure 1. Chart of the nuclides	6
Figure 2. Fission yield of $^{235}\text{U}$ as a function of A and Z	7
Figure 3. Schematic representation of delayed neutron emission	9
Figure 4. Delayed neutron emission in neighboring decay chains	11
Figure 5. TRISTAN layout of the ALRR	13
Figure 6. Fission product generator	14
Figure 7. Long counter neutron detector	19
Figure 8. Schematic of neutron detection electronics	20
Figure 9. Group delayed neutron spectra	26
Figure 10. $^3\text{He}$ cross sections	28
Figure 11. $^3\text{He}$ proportional counter characteristics	34
Figure 12. $^3\text{He}$ proportional counter plateau	35
Figure 13. Schematic of risetime discrimination system	37
Figure 14. Risetime calibration	43
Figure 15. Pulse height calibration	44
Figure 16. Pulse height and risetime response for thermal neutrons	47
Figure 17. $^3\text{He}$ proportional counter energy calibration	50
Figure 18. Typical two-parameter $^{17}\text{N}$ spectrum	55
Figure 19. Final $^3\text{He}$ proportional counter calibration	57

Figure 20.	$^3\text{He}$ ionization chamber shield configuration	60
Figure 21.	Schematic of $^3\text{He}$ ionization chamber electronics	61
Figure 22.	$^3\text{He}$ ionization chamber energy calibration	66
Figure 23.	Decay of neutron activity for mass 137	70
Figure 24.	Decay of neutron activity for mass 138	72
Figure 25.	Decay of neutron activity for mass 88	73
Figure 26.	Decay of neutron activity for mass 89	74
Figure 27.	Decay of neutron activity for mass 93	76
Figure 28.	Comparative $^{17}\text{N}$ spectra	82
Figure 29.	Comparative $^{137}\text{I}$ spectra	88
Figure 30.	Comparative mass 93 spectra	93
Figure 31.	$^{93}\text{Kr}$ and $^{93}\text{Rb}$ spectra	94
Figure 32.	MTC data cycles at detector-1	111
Figure 33.	MTC data cycles at detector-2	113

## LIST OF TABLES

	Page
Table 1. Summary of neutron spectroscopy methods	25
Table 2. Neutron multiscaling conditions	69
Table 3. Half-life measurement results	77
Table 4. Summary of spectrum measurements	78
Table 5. $^{17}\text{N}$ delayed neutron spectrum energies	80
Table 6. $^{137}\text{I}$ delayed neutron spectrum energies	87
Table 7. Delayed neutron spectrum energies of $^{93}\text{Kr}$ and $^{93}\text{Rb}$ in equilibrium	91
Table 8. ISOBAR calculations for mass 93	119

## I. INTRODUCTION

Early in 1939 Roberts, Meyer and Wang (1) observed the delayed emission of neutrons in fission which has come to be called delayed neutron emission. The importance of delayed neutrons in the control of fission chain reactors was recognized by Zeldovich and Khariton (2) more than two years before the first self sustaining chain reaction was achieved. The fundamental role of delayed neutrons in the kinetic behavior, safety, and control of nuclear reactors is a matter of practical experience in hundreds of facilities throughout the world. While the current level of knowledge of delayed neutrons has been adequate to support a growing thermal reactor based nuclear power industry, the next generation of fast breeder reactors will require more detailed knowledge of delayed neutron characteristics in order to operate both safely and efficiently.

One characteristic of delayed neutron emission that is particularly important in the control of fast reactors is the difference in importance or effectiveness of delayed neutrons compared to the prompt neutrons. Since delayed neutrons are emitted at a lower average energy than prompt neutrons, they are reduced in energy to the average reactor spectrum energy more rapidly than the prompt neutrons. Thus the effectiveness or importance of delayed neutrons is enhanced somewhat over the prompt neutrons. The difference in effectiveness is

more pronounced in fast reactors since the average effective energy in a fast reactor spectrum is only one or two orders of magnitude below the initial energy of the delayed neutrons. In thermal reactors the average effective neutron energy is many orders of magnitude below the nascent delayed neutron energy and the difference in effectiveness between prompt and delayed neutrons is much smaller.

Yiftah and Saphier (3) calculated several cases of fast reactor response as a function of delayed neutron effectiveness. The fast reactor systems considered were shown to be marginally stable depending upon the magnitude of the delayed neutron effectiveness. Furthermore, it was shown that present knowledge of delayed neutron spectra is not accurate enough to predict the magnitude of delayed neutron effectiveness in such cases. Thus in fast reactors it is important to know as precisely as possible the energy spectrum of the delayed neutrons emitted from the fission products.

Another important aspect of delayed neutron emission is the identity of the neutron precursors. Traditionally, delayed neutron precursors have been artificially categorized in groups according to a particular half-life (4). Group half-lives were measured by performing an exponential least squares fit to the observed gross delayed neutron decay from an irradiated sample of some particular fissionable isotope. Though such data can be analyzed with any number of groups,

six groups were observed to provide the best fit to the data.

While the group analysis does have some advantage in simplifying reactor kinetics calculations, delayed neutrons do not originate in groups but rather are emitted in the decays of individual precursor nuclei. There are at least 38 known delayed neutron precursors (5). Several authors (5) (6) (7) (8) (9) have demonstrated how the known precursors can best be placed in the traditional group arrangement.

Accurate knowledge of individual delayed neutron precursor characteristics allows formulation of reactor kinetics equations in a new form (10) which accounts for each individual contribution. Knowing the individual contributions allows grouping of precursors based on known data rather than decay curve fitting. Reactor designs which utilize circulating fuel with gaseous fission product release systems make it necessary to know the chemical identity of all delayed neutron precursors to be able to evaluate the control margin of the proposed system.

Finally, the characteristics of the individual delayed neutron precursors can provide highly selective signatures (11) for nondestructive assay of fissionable material management systems.

Another important area of application of the study of delayed neutron precursor characteristics is in nuclear physics. The observation of delayed neutron emission in the

decay of a particular nuclide can be used as a direct test of mass formulas. Talbert, Tucker, and Day (12) have made a comparison between eight recently published mass formulas to determine which ones best predict their observed results.

The measurement of neutron spectra from known emitters can yield information concerning the character of levels above the neutron binding energy of the emitter as well as the spins and parities associated with the levels. The observed neutron spectra can also be used to test the predictions of theoretical models for neutron emission probability values.

With the recent application of laboratory size mass separators operating on-line with fission product emanating targets, it has become possible to study individual fission product nuclides in great detail. TRISTAN (13), the first isotope separator system to operate on-line with a nuclear reactor, is installed and currently is in use at the Ames Laboratory Research Reactor facility. The system has been used with a noble gas fission product generating system (12) to identify six delayed neutron precursors and measure the neutron emission probability of each.

This study deals with recent investigations using the TRISTAN system to study the characteristics of individual delayed neutron precursors emitted by a halogen gas fission product source.

## II. THEORY OF DELAYED NEUTRON EMISSION

A cursory look at the nuclidic chart shown in Figure 1, in which the ordinate is the number of neutrons in the nucleus and the abscissa is the number of protons, reveals the obvious fact that nuclear stability at higher mass numbers requires a proportionally larger number of neutrons than protons. When fission of a high-mass nucleus occurs it is clear that, unless a large number of neutrons are liberated during the fission process, the fission product nuclides will in general contain an excessive number of neutrons. Since the average number of neutrons released in fission of the most common fissile isotope of uranium (i.e.  $^{235}\text{U}$ ) is only about 2.5, it is evident that most of the fission product nuclides are produced on the neutron-rich side of the region of nuclear stability.

The mass and charge distribution of the products of fission have been studied in detail and reported by many authors. The fission yield data of Wahl (14) for thermal neutron induced fission of  $^{235}\text{U}$  has been plotted as a function of both mass number and proton number as shown in Figure 2. The projection on the A-axis shows the familiar double-peaked mass distribution of the fission products consisting of a low-mass region and a high-mass region. The yield is given in percent and represents the total chain yield for a particular mass number.

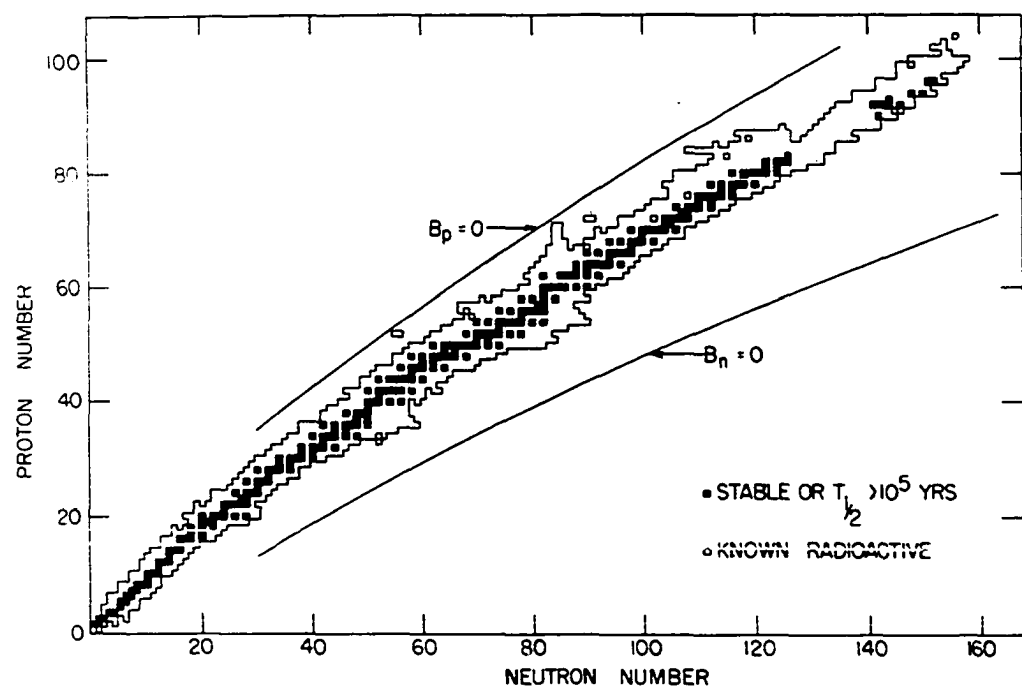


Figure 1. Chart of the nuclides

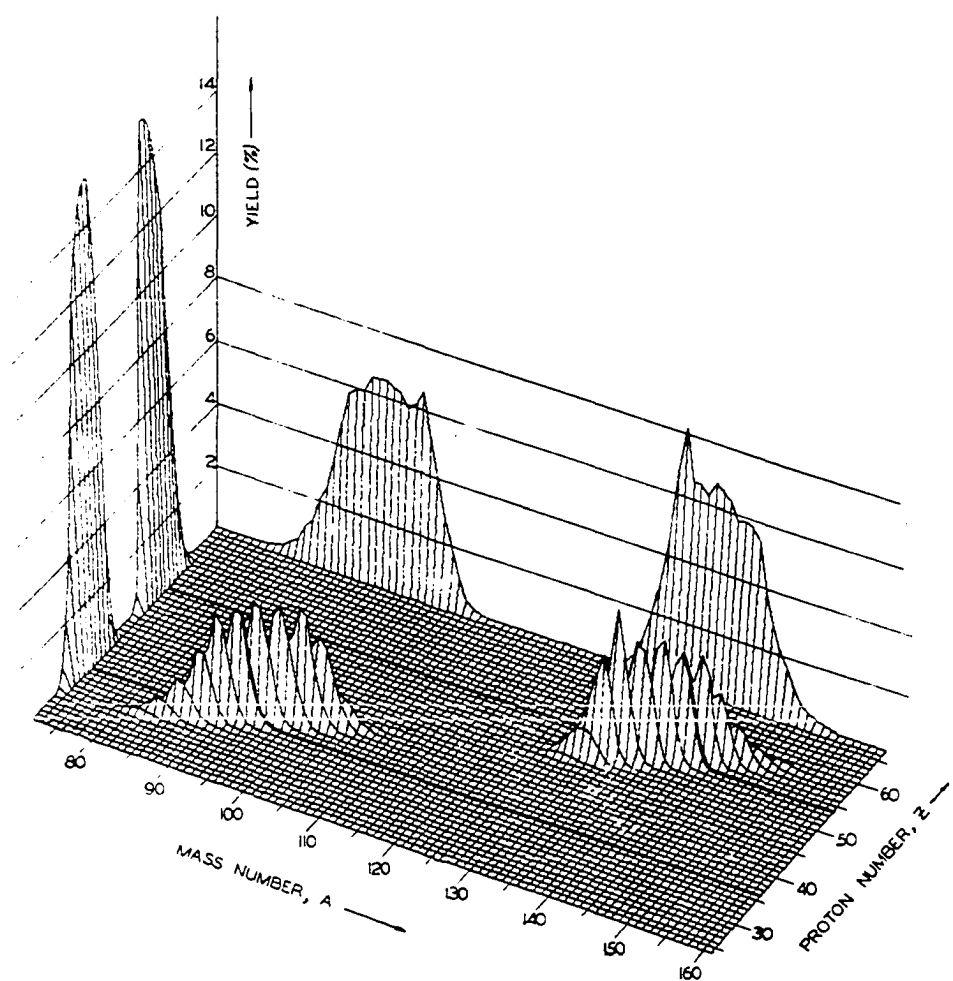


Figure 2. Fission yield of  $^{235}\text{U}$  as a function of  $A$  and  $Z$

When nuclides exist far from the region of stability they are characterized by short half-lives and rather high decay energies. Mass formulas (15) (16) (17) can be used to determine the limits of beta stability, the shape of the nuclear mass surface, neutron binding energies, and decay energies. It is the latter two that are of particular importance in the phenomenon of delayed neutron emission.

The first theoretical explanation of delayed neutron emission was presented by Bohr and Wheeler (18) in 1939. The theory is summarized graphically in Figure 3. Delayed neutron emission involves a precursor, an emitter, and a final nuclide. From Figure 3 it can be observed that the energetics for delayed neutron emission require that the Q-value for beta decay of the precursor be greater than the neutron binding energy of the emitter nuclide. When such is the case a neutron can be emitted promptly by the emitter nuclide. Since there is no apparent delay by the emitter nuclide the neutron activity exhibits the beta decay half-life of the precursor nuclide.

The energy of the emitted neutron is determined by the energy difference between the neutron emitting state above the neutron binding energy in the emitter nuclide and the energy level of the state populated in the final nuclide. Normally, neutron emission goes to the ground state of the final nucleus. The first excited state of the final nucleus is

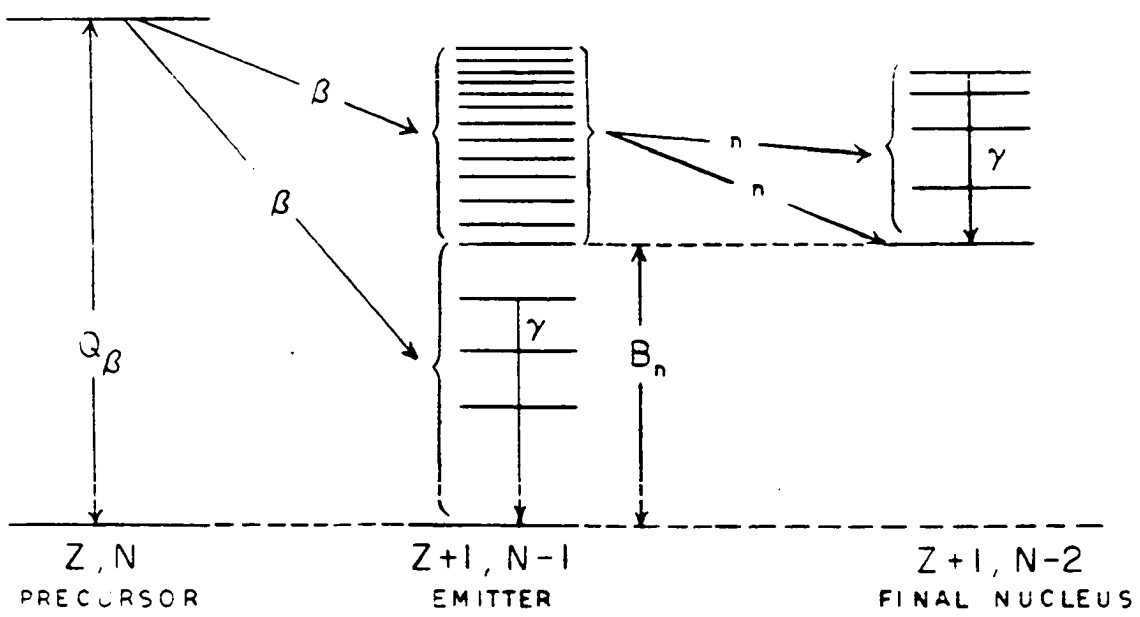


Figure 3. Schematic representation of delayed neutron emission

often between 1 and 2 MeV above the ground state and cannot be populated by neutron emission from the emitter nuclide. In a few cases, however, neutron emission to the first excited state of the final nuclide is energetically possible. The first experimental evidence for this type of delayed neutron emission was observed by Talbert (19) for the decay of  $^{88}\text{Br}$ .

Delayed neutron emission breaks the continuity of the beta decay chain of the precursor nuclide and populates the A-1 decay chain of the final nucleus. In some cases subsequent beta decay can lead to further delayed neutron emission in the A-1 decay chain. Figure 4 gives an example of such a case originating from  $^{93}\text{Kr}$  as the initial precursor. The emitter nucleus  $^{93}\text{Rb}$  populates the ground state of  $^{92}\text{Sr}$  which beta decays to neutron emitting levels in  $^{92}\text{Sr}$ . Such cases of secondary delayed neutron emission are usually relatively unimportant. In this example the number of neutrons emitted by  $^{92}\text{Sr}$  is proportional to the products of the neutron emission probability values for both  $^{93}\text{Rb}$  and  $^{92}\text{Sr}$ . However, in case the fission yield and neutron emission probability for the emitter nuclide in the mass A decay chain are large and the fission yield for the A-1 decay chain is small, secondary delayed neutron emission may result in a significant contribution to the number of neutrons emitted by the A-1 decay chain.

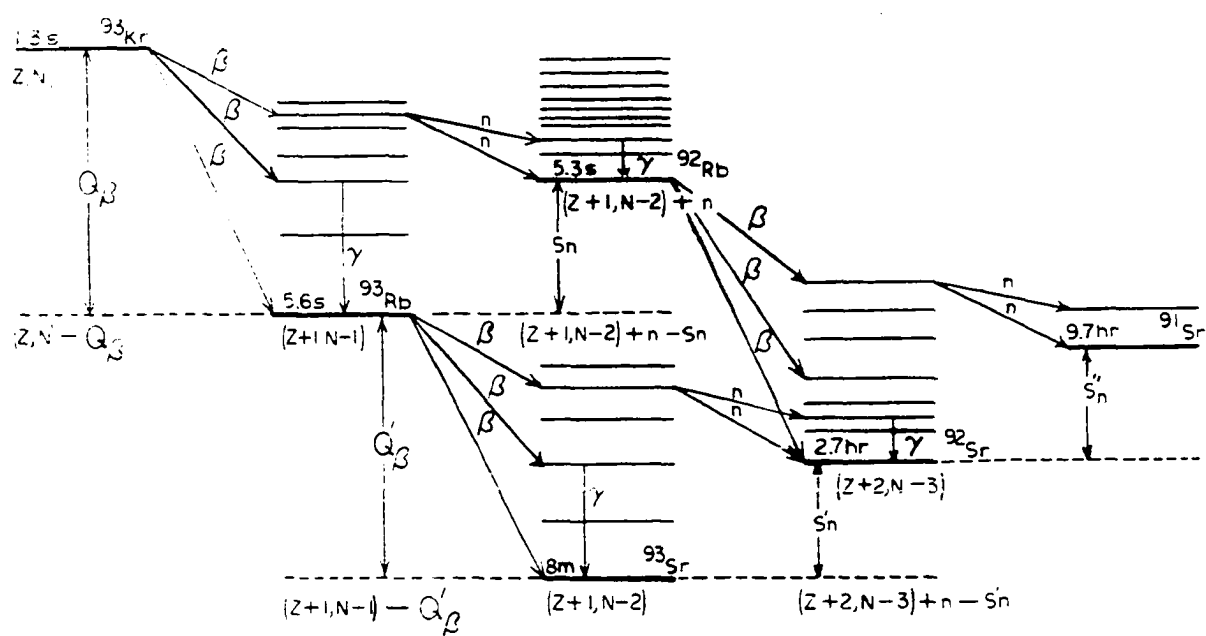


Figure 4. Delayed neutron emission in neighboring decay chains

### III. EXPERIMENTAL METHODS

#### A. The TRISTAN Mass Separator Facility

The TRISTAN mass separator facility was the first of its type to be connected on-line to a nuclear reactor (13). The facility was designed to produce mass-separated fission products on a continuous basis and deliver them to a convenient deposit point for study by suitable detection methods.

Figure 5 shows the general layout of the facility in its current configuration at the Ames Laboratory Research Reactor (ALRR).

The fission product generator (FPG) is housed in a large shielded cavity which is located adjacent to face 6 of the reactor pedestal. When not in use the horizontal beam tube at face 6 is filled with water and its pneumatically actuated beam shutter is closed. The FPG consists of an aluminum can containing shallow trays as shown in Figure 6. The FPG is shown with the back plate removed and placed to the left in the figure. The trays are loaded with uranyl stearate [ $\text{UO}_2(\text{CO}_2\text{C}_{17}\text{H}_{35})_2$ ] containing about 2 gm  $^{235}\text{U}$ . The choice of uranyl stearate for the  $^{235}\text{U}$  matrix was determined by its known property of strong gaseous emanation (20). The can is closed with an O-ring sealed lid and has a sweep gas inlet line, a vacuum gauge connection, and an outlet line at the top of the back plate which connects via a transport line to

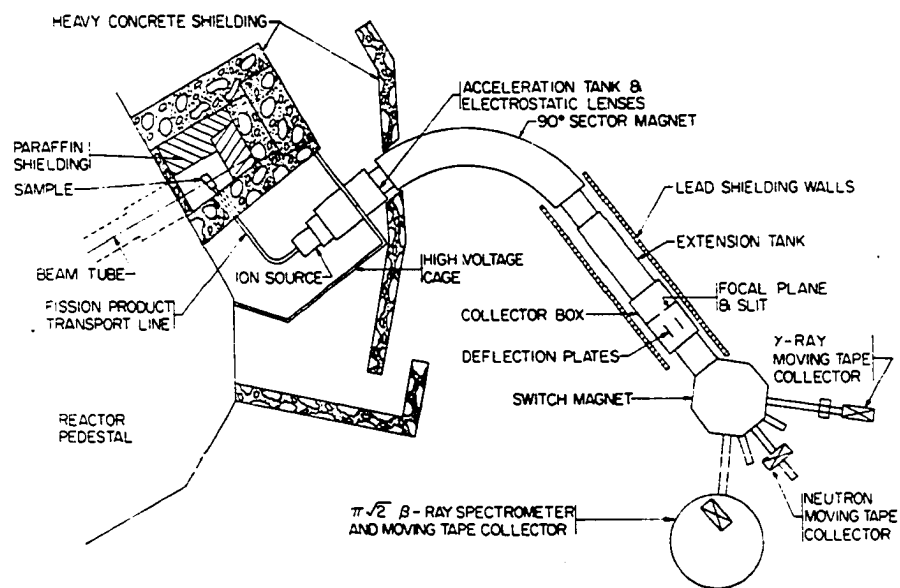


Figure 5. TRISTAN layout at the ALRR

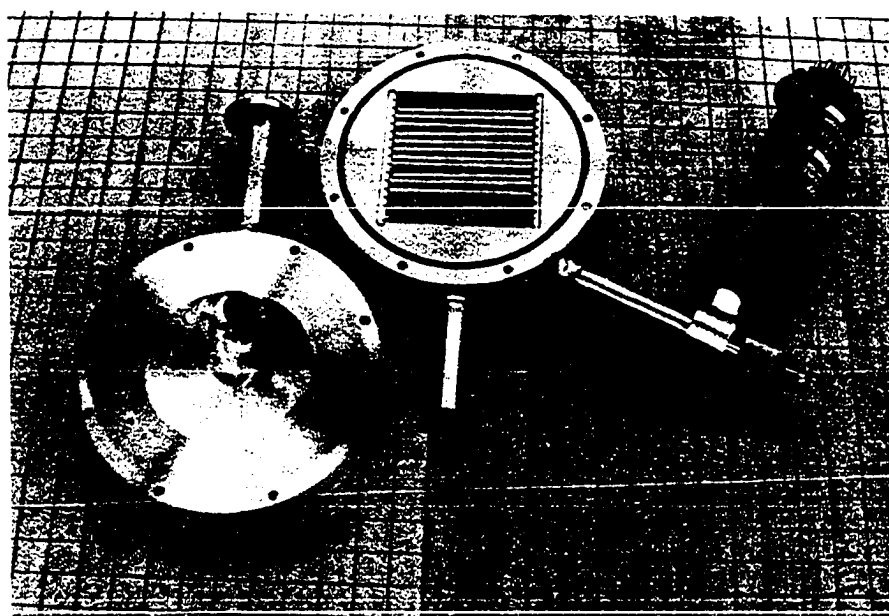


Figure 6. Fission product generator

the inlet of the mass separator ion source. The FPG is operated at high vacuum and at the 50 kv mass separator acceleration potential; thus adequate electrical insulation must be provided between the can and the shield cavity which is at ground potential.

The FPG is mounted on the centerline of the face 6 beam tube approximately 20 cm from the beam shutter face. When the beam tube water shield is removed and the shutter is opened the total neutron flux at the position of the FPG is about  $3 \times 10^9$  neutrons per  $\text{cm}^2\text{-second}$ , with thermal neutrons contributing about 75% of the total.

The fission products emanating from the FPG are carried to the mass separator ion source both by pressure differential and the action of a "sweep" gas which is introduced into the FPG to aid in supporting the plasma discharge in the ion source. The ionized gaseous fission products are extracted by an electrostatic lens system, while the neutral output of the ion source is pumped to the radioactive gas discharge system of the ALRR via the separator vacuum system.

The electrostatic lens system shapes the beam of ionized particles for injection into the  $90^\circ$  sector magnet. The magnet portion of the system separates the ionized particles according to mass and focuses the mass-separated ion beams in sharply defined lines in the collector box. The collector box contains a potassium bromide screen which can be lowered

into the focal plane for viewing the beam to facilitate tuning the separator. The separation between the beam of adjacent mass numbers at the focal plane is on the order of 1 to 2 cm depending upon the mass region being viewed. Thus to select the mass beam to be studied it is sufficient to provide an aluminum mask at the focal plane with a narrow vertical slit which will pass the mass beam desired and block all higher and lower mass beams. Thus for on-line studies, the mass selection is made in the collector box.

The selected mass beam then passes into the switch magnet which may direct the beam to one of five ports. The switch magnet ports lead into the specialized detection equipment which is used to analyze the radioactive component of the beam.

For these studies two of the switch magnet ports were used. Early measurements were made using the 22.5° port adjacent to the moving tape collector. Recent measurements have been made using the straight-through port. An additional horizontal compression lens was mounted on the back of the switch magnet to reduce horizontal dispersion and direct the beam into a modified moving tape collector which was originally designed for beta spectroscopy studies.

The TRISTAN system has been developed to a high degree of automation which greatly facilitates its operation. It is equipped with a beam stabilization system which corrects for

changes in the 50-kV acceleration potential and maintains the selected beam at the proper position for passage through the collector box slits. A flux monitoring device in the 90° sector magnet is used to measure the magnetic field which is then combined with the measured ion acceleration potential to electronically calculate and display the mass number of the beam selected. In addition, an electronic beam scanning device is incorporated in the collector box which displays the shape of the beam on an oscilloscope at the mass separator console. These innovations are examples of why the TRISTAN system is perhaps the finest on-line separator system in the world.

#### B. Precursor Identification

One method of identifying delayed neutron precursors makes use of the fact that delayed neutron emission is delayed by the beta decay process. Thus the neutron emission rate reflects the beta decay half-life of the precursor. In cases where the half-life of the precursor is known, measurement of the neutron emission rate will serve to identify the precursor. It is possible that the accuracy associated with the precursor half-life may be improved by observing the delayed neutron emissions provided the neutron detector is insensitive to interfering gamma and beta activities.

In these studies delayed neutron emission half-lives were measured using the calibrated neutron detector two views of which are shown in Figure 7. The detector, which is referred to as a "long counter", consists of five boron trifluoride-filled proportional counters embedded in a block of paraffin. The front face of the detector has a recessed port 15 cm deep to allow the counter to be slipped over the end of the beam tube containing the activity deposit point which extends from the switch magnet of the separator system. A 5-cm layer of boron-loaded paraffin on all sides of the detector array is incorporated in the detector to shield against room neutron background. The detector assembly is contained in an aluminum case and mounted on a movable rack. The rack contains all of the associated high voltage and preamplifier power supplies as well as the pulse summing and shaping electronics for the detector. The detector rack is thus a self contained unit which requires 115 VAC input and provides a pulse output shaped for analysis by a multichannel analyzer (MCA). Figure 8 is a schematic representation of the neutron detector system. The detector was designed to have a detection sensitivity which is independent of neutron energy. The energy response was measured using two calibrated neutron sources, an AmLi source for the low energy region and a PuBe source for the high energy range. The observed absolute detector efficiency was found to be

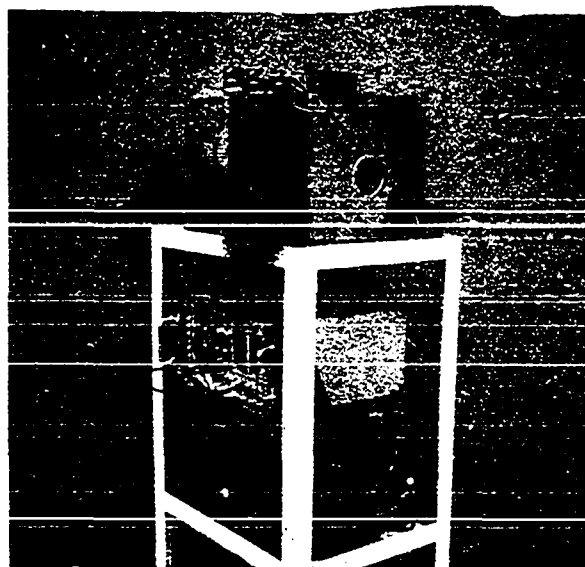
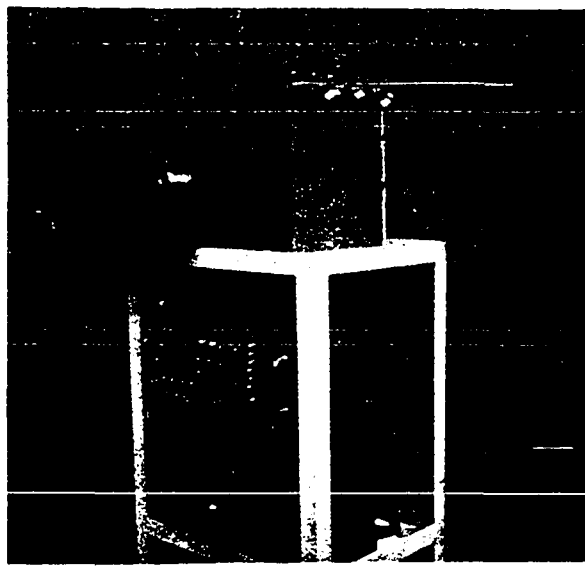


Figure 7. Long counter neutron detector

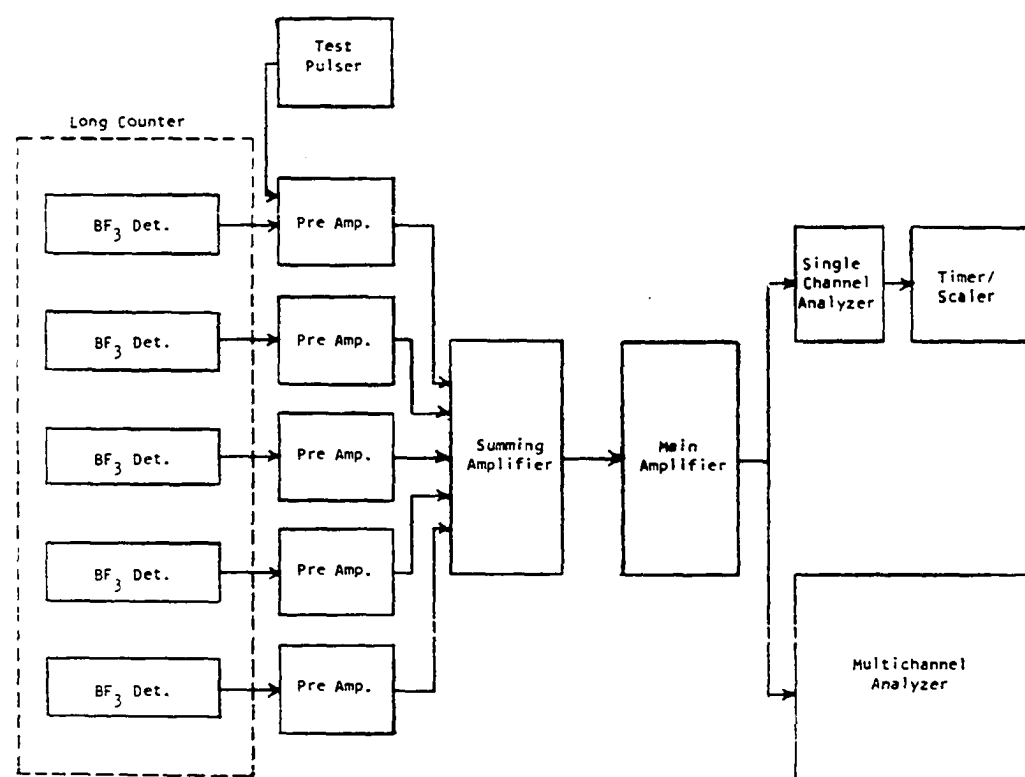


Figure 8. Schematic of neutron detection electronics

$2.82 \pm 0.21\%$ .

For a typical measurement the detector was positioned over the switch magnet beam deposit tube and the detector pulse output was connected to a MCA set to accumulate data in the time multiscaling mode. The separator was then tuned to the desired mass and the beam was focused on the activity deposit point. With the activity maximized by fine tuning of the separator the equilibrium neutron count rate was observed to estimate the signal to background ratio to be expected in the multiscaling run. Next the MCA was connected to an automatic sequencing device called the Daughter Analysis Control (DAC). The DAC may be programmed to turn the MCA on and off at selectable times and to begin and end beam deposit by controlling the high voltage applied to a set of beam deflection plates located in the separator collector box. The DAC was set to collect activity for several half-lives then simultaneously deflect the beam and turn on the MCA which then multiscaled the detector count rate at a preselected time per channel. After multiscaling for a time equivalent to about five half-lives the DAC stopped the MCA, reset it to channel zero and began another beam deposit sequence. The cycle was repeated until the multiscaling decay curve contained a minimum of 10,000 counts per channel at the end of collection.

The data from the completed runs were printed out and key punched in proper format to be read into the half-life fitting program SMASH (21). The program output includes the number of half-lives fitted to the decay curve, the fitted value of the half-life, the fractional amount of each half-life component at the start of the decay curve, the fitted background level, a statistical evaluation of the fit and a graph of the input data with the fitted decay curve superimposed over the data points.

The time multiscaling method of precursor identification is most effective when the signal-to-background ratio is as high as possible at the beginning of the decay period. The equilibrium neutron activity of a particular precursor is dependent upon the efficiency of the separator system for delivery of the precursor to the neutron counting port and the neutron emission probability of the precursor. There are a number of precursor nuclides which, due to one or both of the above reasons, are found to produce a low level of neutron activity (i.e. equal to background or less) at the neutron counting port. For nuclides in this category the signal-to-background ratio may be on the order of one or less. Thus, to obtain meaningful results using time multiscaling techniques extremely long separator run times would be required.

### C. Emission Spectra

The measurement of differential neutron spectra has presented substantial difficulties since the discovery of the neutron. The very nature of the neutron precludes the use of momentum or velocity measurements based on interactions with electric or magnetic fields. Thus neutron detection is an indirect process that requires an exchange medium or particle with suitable detection properties from which information about the energy of the neutron can be inferred.

In view of the nature of the neutron energy detection process, no single method exists which has been found to be suitable for all neutron spectra applications. Thus, a number of different methods have been developed which in general are tailored to the requirements of the particular measurement to be made. However, all of the methods for determining differential neutron spectra can be divided into three groups:

1. Time-of-flight methods,
2. Recoil processes,
3. Neutron-induced nuclear reactions.

The choice of a particular neutron spectroscopy method depends upon: (1) the energy range to be covered, (2) the energy resolution required, and (3) the detection efficiency needed. The recent work by Werle (22) contains an excellent summary of available neutron spectroscopy methods as applied

to the measurement of radioactive neutron source spectra. Werle concluded that the proton recoil proportional counter was best suited for the measurement of neutron source spectra. Table 1 presents a summary of some existing neutron spectroscopy methods and characterizes the methods by type, energy range, energy resolution, and detection efficiency.

From the early delayed neutron group spectra measurements of Bachelor and McHyder (23) shown in Figure 9, it can be observed that gross delayed neutron emission spectra extend over an energy range of near zero to about 2 MeV. Also the suggestion of structure in the spectra is apparent. It is clear that the same general characteristics should be applicable to the spectra of the individual delayed neutron precursors which sum together to yield the group spectra of Figure 9.

The neutron spectroscopy method best suited for the measurement of individual delayed neutron emission spectra should thus cover the energy range from zero to 2 MeV with the best possible resolution and the highest efficiency. From Table 1 there are three possible candidates; (1) Proton recoil proportional counter, (2)  $^3\text{He}$  proportional counter, (3)  $^3\text{He}$  ionization chamber. The choice between the three required a compromise between the better energy range of the proton recoil proportional counter and greater efficiency of the  $^3\text{He}$  proportional and ionization counters. Since the

Table 1. Summary of neutron spectroscopy methods

Type	Method	Energy Range (MeV)	Energy Res. (%)	Detection Eff.*
Time-of-flight	Time-of-flight	<1	**	L
Proton recoil	Scintillators	0.5-15	10	H
	Nuclear emulsions	>0.5	3	L
	Telescopes	>1	**	L
	Prop. Counters	0.01-10	10	L
Nuclear reaction	$^6\text{Li}$ semiconductor	>0.5	**	L
	$^3\text{He}$ semiconductor	>1	**	L
	$^3\text{He}$ prop. counter	0.1-2	<5	M
	$^3\text{He}$ ion. chamber	0.1-2	<3	M

\* H= 1 to 100%, M= 0.001 to 1%, L= <0.001%.

\*\* Resolution is strongly dependent upon the experimental setup.

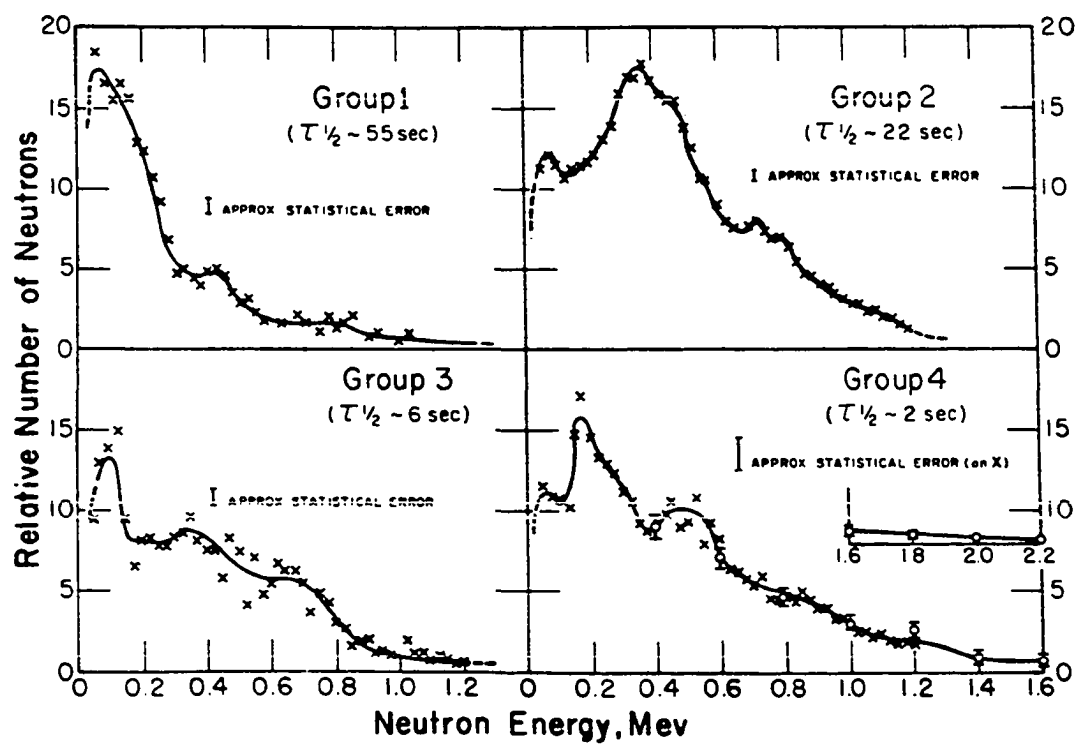
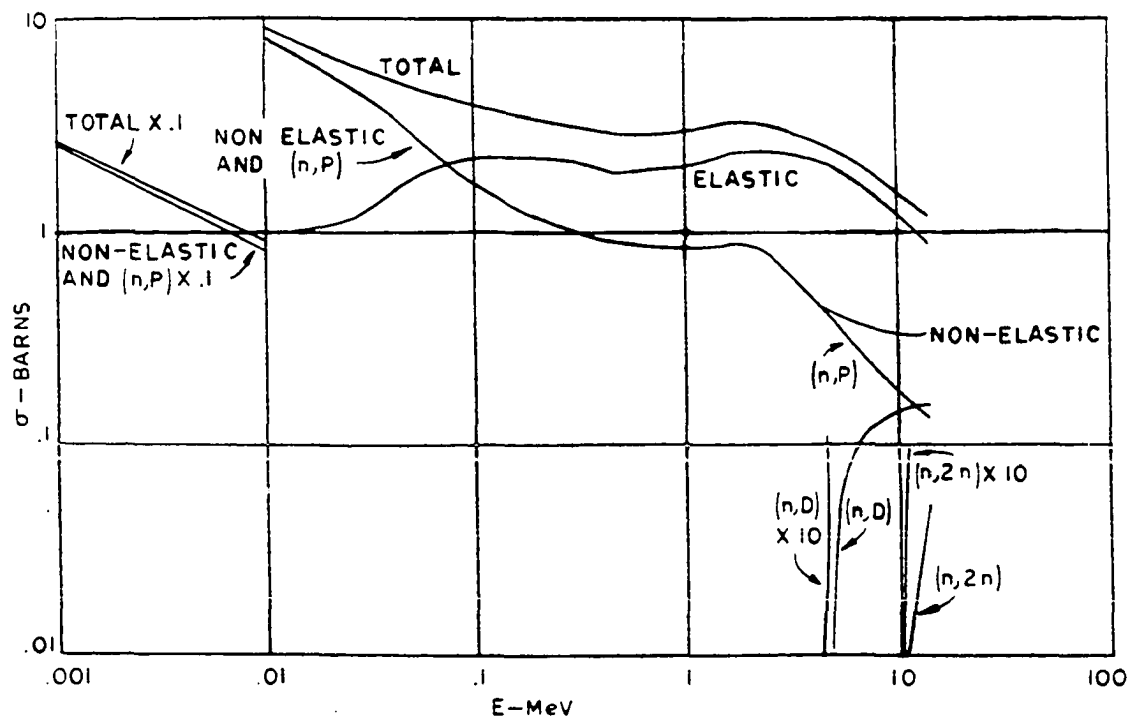


Figure 9. Group delayed neutron spectra

equilibrium neutron source strengths of the individual precursors observed during the half-life measurements were quite small (ranging from a minimum of about  $5 \times 10^2$  neutrons per second to a maximum of about  $3 \times 10^4$  neutrons per second at the beam deposit point of the neutron counting port), the greater efficiency of the  ${}^3\text{He}$  detectors was judged to be more important than the low energy range sensitivity of the proton recoil proportional counter.

#### D. Spectrometer Calibration Techniques

The operation of both the  ${}^3\text{He}$  proportional counter and  ${}^3\text{He}$  ionization chamber is based on the exothermic  ${}^3\text{He}(n,p)\text{T}$  reaction which has a Q value of 0.764 MeV. The cross section for the reaction is well known over the energy range 0.001 eV to 14 MeV (24). In addition to the  $(n,p)$  reaction, elastic scattering can occur between the incoming neutrons and the  ${}^3\text{He}$  nuclei in the counter. Furthermore, as the incoming neutron energy increases additional threshold reactions can occur. A plot of the comparative cross sections of the various measured  ${}^3\text{He}$  reactions is shown on Figure 10. The first of the threshold reactions occurs at energies greater than 4 MeV which is well above the range of neutron energies emitted as delayed neutrons. Thus the only processes of interest for delayed neutron spectra measurements are the  $(n,p)$  and elastic scattering reactions.

Figure 10.  ${}^3\text{He}$  cross sections

If the neutrons involved in the  ${}^3\text{He}(n,p)\text{T}$  reaction are monoenergetic, then the observed pulse height spectrum from the counter will exhibit a peak at a pulse height proportional to  $E + Q$ , where  $E$  is the incoming neutron energy, provided the reaction products expend all of their energy within the active volume of the detector. If either one or both of the reaction products strikes the counter wall before depositing its energy in the active detector volume a pulse will be generated which has a pulse height less than the full-energy pulse. The effect of such "wall effect" pulses is to create a low energy tail on the full-energy peak. (The magnitude of the wall effect in any particular detector is strongly dependent upon the detector design.) For the same incident neutron energy the elastic scattering reaction,  ${}^3\text{He}(n,n){}^3\text{He}$ , will result in a continuous distribution of pulse heights up to a maximum of  $0.75E$ . Finally, the pulse height spectrum will also exhibit a relatively large thermal neutron peak at a pulse height corresponding to 0.764 MeV.

The recoil distribution can begin to interfere with the resolution of low-energy neutron peaks when the maximum recoil energy is greater than the energy of the thermal neutron peak. From the relationship  $0.75E > Q$  it is apparent that recoil pulse interference can occur for  $E > 1.02$  MeV. Therefore special calibration techniques are required to account for the recoil distribution when neutrons having ener-

gies greater than 1.02 MeV are incident upon the detector. Similarly, wall effect pulses can interfere with the resolution of all neutron peaks below the highest peak in the spectrum and the calibration technique must be adequate to deal with this problem.

There are two basic approaches to the problem of calibrating the energy response of a  $^3\text{He}$  detector. The first approach involves making use of differences in the electronic characteristics of the pulses originating in the detector and by suitable electronic processing rejecting all pulses except those corresponding to the full-energy peak. Sayers and Coppola (25) used such an approach when they demonstrated that the difference between pulse risetimes of recoil events and reaction events could be used to discriminate against the recoil pulses. More recently Izumi and Murata (26) showed that pulse risetime could also be used as a basis for discriminating against wall effect pulses.

The other basic approach to  $^3\text{He}$  detector calibration involves determining the detector response function as a function of incident neutron energy either by calculational methods or by direct measurement with monoenergetic neutron sources and unfolding the raw spectra using an appropriate inversion matrix or spectrum stripping technique. The work of Wang (27) is an example of the analytical calibration technique in which the magnitude and energy distribution of

pulses due to wall effects, recoil events, and threshold reactions are calculated based on the known detector configuration and the incident neutron energy. Greenberger and Shalev (28) describe a calibration method based on the direct measurement of the detector response function at several different energies using monoenergetic neutron sources. The measured response functions are then used to generate continuous analytical expressions which describe the detector response as a function of energy to facilitate spectrum stripping beginning with the highest energy peak in the spectrum.

For this study both a  ${}^3\text{He}$  proportional counter and a  ${}^3\text{He}$  ionization chamber were purchased and their use as neutron spectrometers evaluated. A risetime discrimination system was developed for use with the  ${}^3\text{He}$  proportional counter. The  ${}^3\text{He}$  ionization chamber was supplied with response function measurements for seven different monoenergetic neutron energies over the range from 0.2-1.6 Mev. A description of each of the detectors and the methods used for energy response calibration follows.

#### 1. ${}^3\text{He}$ proportional counter

The  ${}^3\text{He}$  proportional counter used for this work was a Texas Nuclear Model 9341, containing 4 atmospheres  ${}^3\text{He}$  and 2 atmospheres Kr. The counter is cylindrical in shape having a nominal 2 inch outside diameter and a 6-inch active length.

The outer wall of the detector is made of stainless steel and served as the cathode. The anode wire extends along the central axis and is maintained at a positive potential with respect to the cathode by a high voltage connector feed-through which is mounted on one end of the detector. The detector was equipped with both a thermal neutron and gamma shield. The neutron shield is in the form of a tight fitting open topped can with an inside diameter slightly larger than 2 inches and length about 8 inches. The can was constructed from 0.030-inch Cd sheet and the seams were electron beam welded. The gamma shield was turned from a single Pb ingot in the form of an open topped can with a 0.5-inch nominal wall thickness, 2.125-inch inside diameter and 8.5-inch overall height. The shields are removable to facilitate periodic calibration checks using a thermal neutron source.

The calibration process consisted of three phases: (1) determination of detector characteristics, (2) assembly and calibration of risetime discrimination system, and (3) calibration of the complete spectrometer system by measuring the spectra of neutron sources with known energy distributions.

The measured gas amplification and thermal-peak resolution characteristics for the detector are shown in Figure 11. The measurements were made using a well moderated PuBe neutron source with the thermal neutron and gamma shields removed from the detector. The detector was connected to a suitable preamplifier and the preamplifier output was fed to a main amplifier. The main amplifier output was connected to a multichannel analyzer (MCA) set to operate in the pulse height analysis mode. High voltage was applied to the detector via the preamplifier high voltage connection and the system gain and thermal peak resolution were measured for various bias settings. The same electronics setup was then used to measure the detector plateau characteristics shown in Figure 12. The plateau curves were strongly dependent upon the system threshold and gain.

It should be noted that the plateau curve is created when the response function of the detector is swept through the effective window of the system. Therefore, when the bias on the detector is increased, counts begin to be observed as the thermal neutron peak becomes greater than the system threshold due to gas multiplication. As the bias is increased further the observed count rate remains fairly constant while the thermal peak passes through the range of the effective system window. Finally, the observed count rate begins to increase rapidly with continued bias increase as

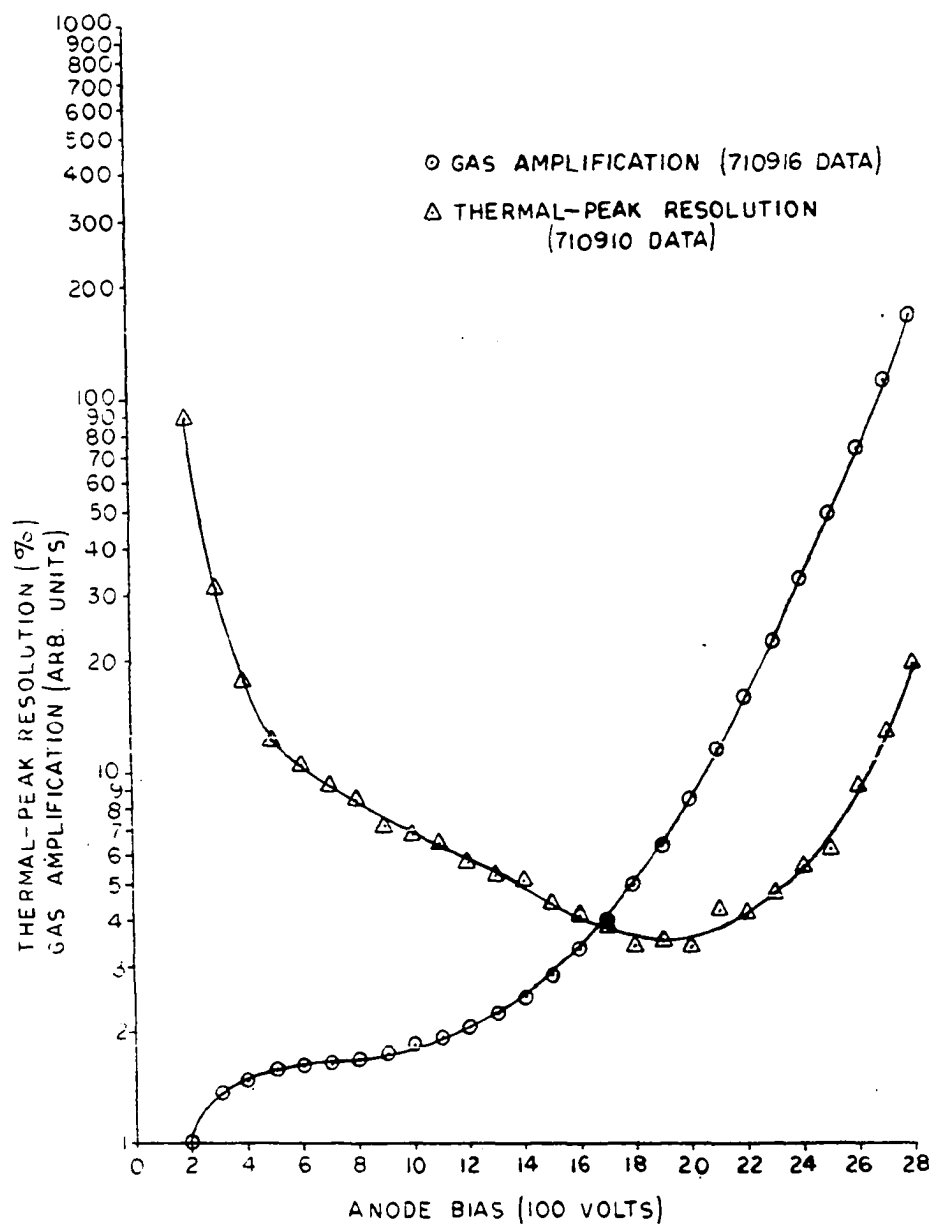


Figure 11.  ${}^3\text{He}$  proportional counter characteristics

○ GAIN=100X1, THRES=1/2 PEAK(Th)  
CALIB=.0018 MeV/CH at 1900 V.

△ GAIN = 50X.917, THRES=1/2 PEAK(Th)  
CALIB=.004 MeV/CH at 1900 V.

▽ GAIN = 50X.917, THRES=1/4 PEAK(Th)  
CALIB=.004 MeV/CH at 1900 V.

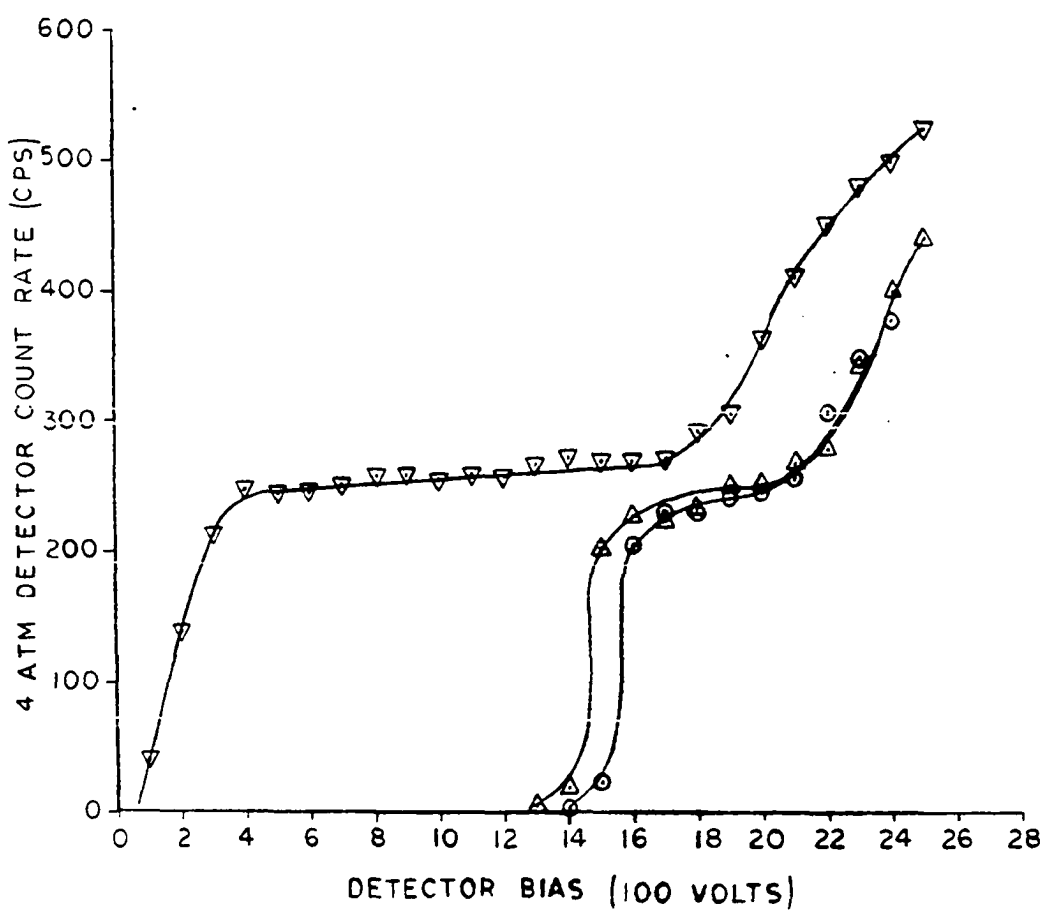


Figure 12.  ${}^3\text{He}$  proportional counter plateau

the low-level noise of the detector response is amplified above the system threshold. The system window can be set by an actual single channel analyzer (SCA) module, or by the effective window of the system which is controlled by the voltage response range of the electronics, or the multichannel analyzer analog-to-digital converter (ADC).

The operating bias for the detector was chosen as 2100 volts in order to maximize the gas multiplication and at the same time maintain the thermal peak resolution and plateau operating point at acceptable values.

A schematic diagram of the risetime discrimination system developed for use with the  $^3\text{He}$  proportional counter is shown in Figure 13. The system was arranged to process each pulse originating in the detector by simultaneous analysis of the pulse risetime and magnitude such that signals proportional to the pulse risetime and magnitude were delivered to the two-parameter analyzer ADC's in coincidence. The system is similar to that developed by Izumi and Murata (26) except that the risetime analysis uses an improved version of the "10%-90% level pick off" method developed by Kinbara and Kumahara (29). Furthermore, in this system strobed biased amplifiers have been incorporated in both the pulse height and risetime channels. The biased amplifier in the pulse height channel is used to store pulse height information until the ADC is ready to accept data. The biased amplifier

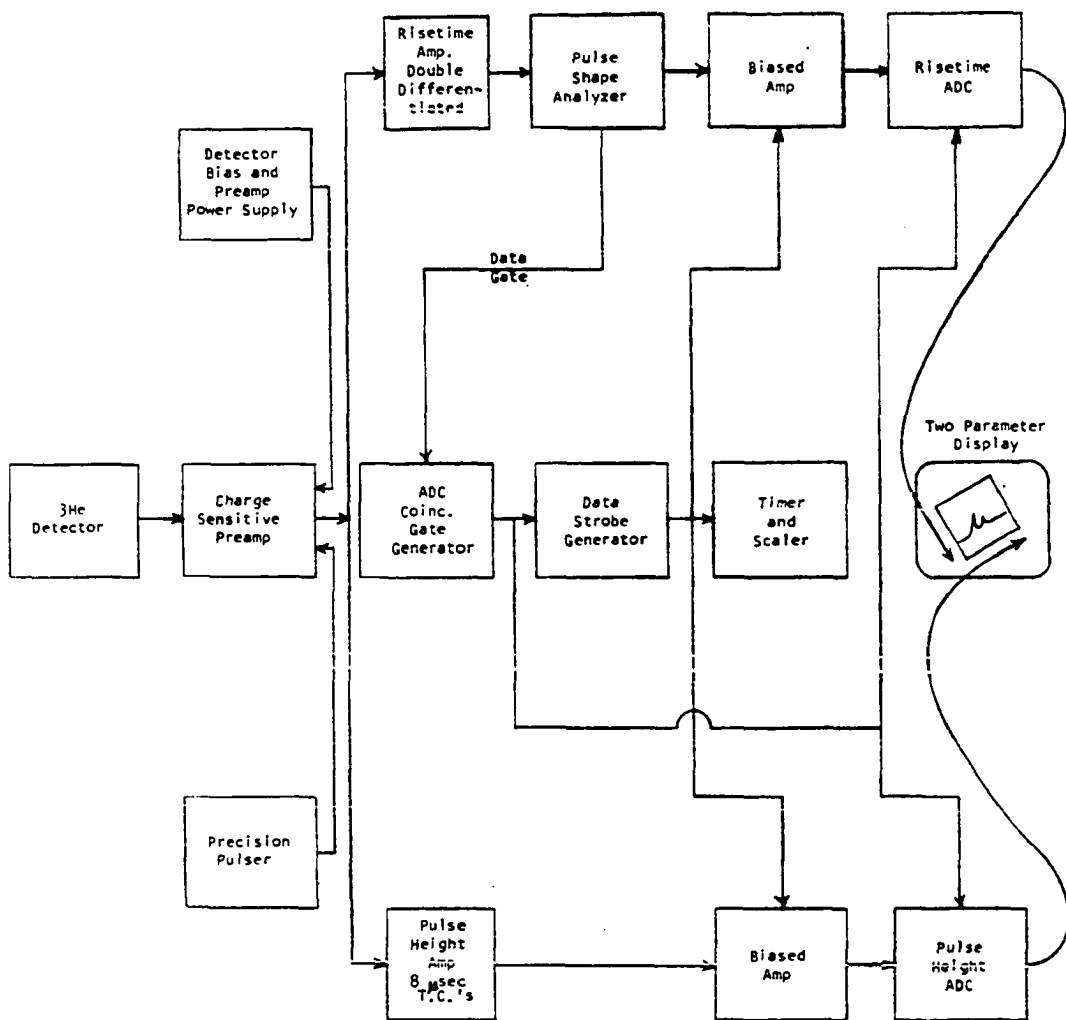


Figure 13. Schematic of risetime discrimination system

in the risetime channel serves the dual purpose of linearizing the system risetime response as well as storing pulse height information proportional to risetime until the ADC is ready to accept data. The system stores both channel outputs in a two-parameter coincidence spectrum. Details of the equipment used for the system appear in Appendix B.

The system was calibrated using a precision pulse generator which had switch selectable risetimes of 0.5, 1.0, 2.0, and 5.0 microseconds. The pulse generator input to the system was at the test input of the charge sensitive preamplifier. The system shown in Figure 13 operates in the following manner.

The output of the preamplifier is divided into two channels, the upper channel on the diagram being the risetime analysis portion and the lower channel, the pulse-height portion of the system. The pulse timing electronics and count rate indicator are shown in the middle of the diagram.

The risetime analysis begins at the double differentiation amplifier. The first differentiation was set at 0.8 microseconds and the second differentiation was set at 3.2 microseconds. These values yielded a second differentiation to first differentiation ratio of 4 which is larger than the value of 2.5 recommended by Cuttler et al. (30) for optimum risetime analysis using the zero cross-over method. However, it was observed that the time con-

stants used yielded an amplifier pulse output with the most desirable characteristics for the pulse shape analyzer.

The pulse shape analyzer used was a commercially available unit (ORTEC Model 458). The device measures the fall time of the input pulses and generates a rectangular output pulse with height proportional to the time required for the input pulse to drop from 90% to 10% of its peak value. The Kinbara and Kumahara (29) method of risetime analysis was developed to avoid the noise problems involved in using the zero cross-over of a double differentiated pulse as a measure of the input pulse risetime. Kinbara demonstrated that the time required for the leading edge of a double differentiated pulse to rise from 10% to 90% of its peak value was directly proportional to the input pulse risetime. If the double differentiated pulse is symmetrically shaped by proper adjustment of the differentiation time constants then the pulse falltime between 90% and 10% will likewise be proportional to the input pulse risetime. This method has the advantage that the full magnitude of the pulse is determined before the risetime analysis begins and thus pulses outside of desired pulse height limits can be rejected without further analysis.

The biased amplifier accepts the rectangular pulses from the pulse shape analyzer and stores the pulse magnitude until the output is strobed out to the ADC in coincidence with the pulse height channel by the data strobe line. It should be

noted that although the magnitude of the pulse shape analyzer output exhibits a linear relationship to pulse risetime, the line in general has a non-zero intercept. By proper adjustment of the amplifier bias the desired zero intercept linearity can be achieved.

The pulse height analysis channel begins with an amplifier which integrates the pulse from the preamplifier using an 8 microsecond time constant. The function of the amplifier is to generate a pulse whose height is independent of input risetime and carries only information about the magnitude of the input pulse.

The biased amplifier in the pulse height channel stores the pulse height information from the integration amplifier until the output is strobed out to the ADC in coincidence with the risetime channel.

It is important to note the significant time difference that exists between the two channels. The risetime channel processes a pulse and delivers the risetime information to its biased amplifier within about 5 microseconds. The pulse height channel, however, requires about 12 microseconds to determine the pulse height and deliver the pulse to its biased amplifier. Since the two-parameter analyzer coincidence gate must be narrow to prevent storage of non-coincident events, it was necessary to carefully time the data delivered by the two channels to the ADC's. This was

accomplished by the two gate generators. The input to the gate generators was taken from the input discriminator of the pulse shape analyzer; the line marked "Data Gate". The pulse shape analyzer input discriminator was set at a value which essentially eliminated all pulses arising from gamma induced events within the detector. Thus the data gate was generated only for neutron induced pulses. The signal was input to the gate and delay generator which delayed the data gate for the proper length of time and then generated a coincidence gate pulse to open the coincidence gates on the ADC's. The coincidence gate pulse was also input to a second gate and delay generator which delayed the gate for a sufficient length of time to satisfy the ADC coincidence input requirements and then generated a data strobe pulse which strobbed out the information in both biased amplifiers into the open ADC's. At the termination of the ADC coincidence gate pulse (about 4 microseconds) the system was ready to analyze another pulse.

The information in the ADC's was then processed by the two-parameter, multichannel analyzer system, stored in the analyzer memory and displayed on an oscilloscope in an isometric format showing counts per channel as a function of both pulse height and risetime.

The full 4096 channel memory of the two-parameter analyzer was used for data storage. The two-parameter stor-

age was programmed for a 16x256 array with the risetime information being digitized into 16 slices containing 256 channels of pulse height information per risetime slice.

In order to calibrate the risetime system the precision pulser was set to a given output pulse height, the pulse risetime was set at a particular value, and the risetime slice where data storage occurred was noted. The process was repeated for each of the selectable risetimes. The data were then plotted to determine the zero intercept. If a non-zero intercept was observed the amplifier bias was changed and the test was repeated. Figure 14 shows the risetime calibration results with pulse risetime plotted versus risetime slice number and the amplifier bias set to yield a zero intercept.

The pulse height channel was calibrated in a similar manner by fixing the input pulse risetime and varying the amplitude. Figure 15 is a plot of pulse amplitude versus pulse height channel number. A least square linear fit through the points gave a zero-energy channel of -16.89.

A final calibration test was performed to verify that the risetime and pulse height channels were independent. The test was performed by taking 10-second analyzer runs on all possible combinations of pulse generator settings using risetimes of 0.5, 1.0, 2.0, and 5.0 microseconds and pulse amplitudes measured at the main pulse height channel amplifier of 1, 2, 3, 4, and 5 volts. The results showed

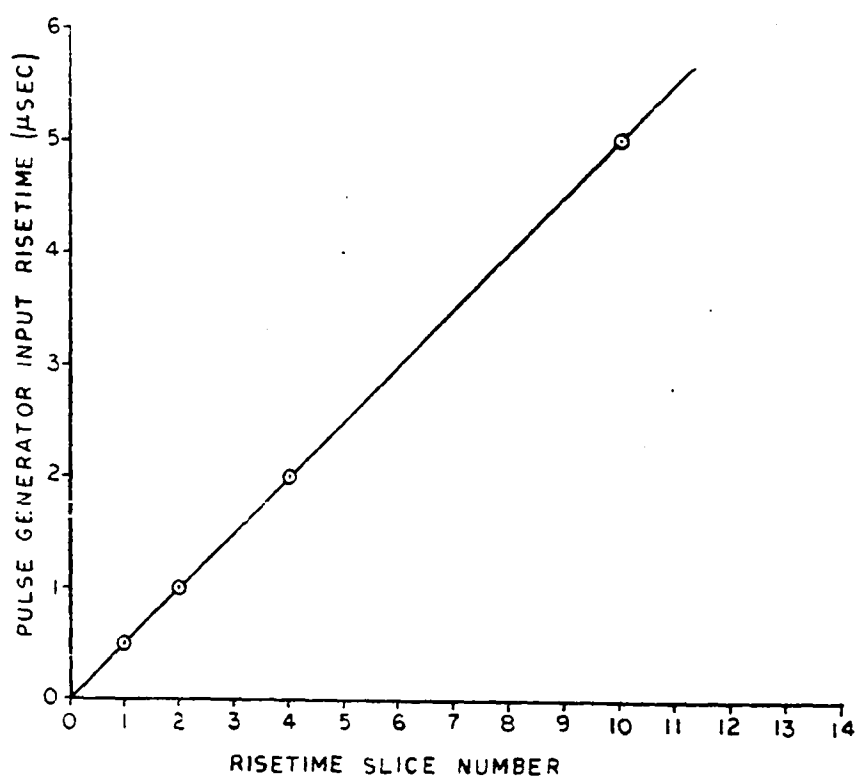


Figure 14. Risetime calibration

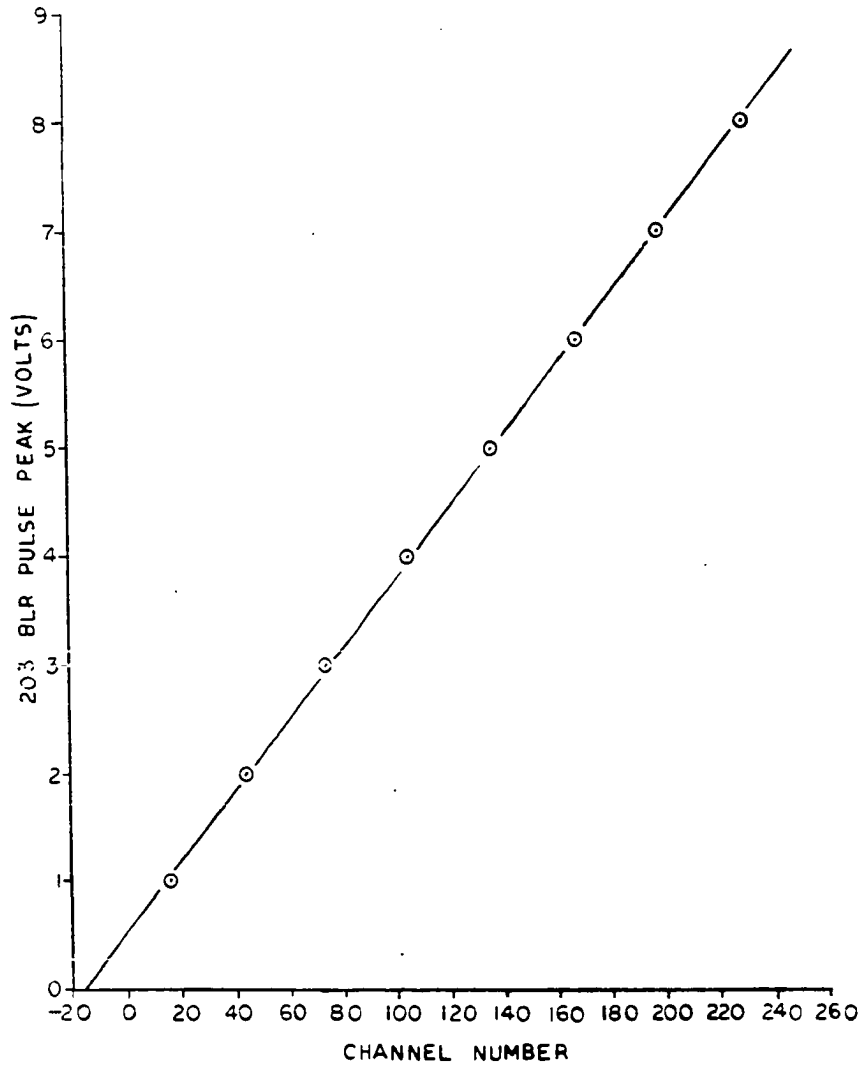


Figure 15. Pulse height calibration

that the pulse height channel number remained constant for each voltage setting of the pulser while the risetime was varied over the test range, and that the risetime channel remained constant for each selected risetime setting while the pulser amplitude was varied. The two-parameter calibration spectrum was taken in the "two-parameter plus profile" mode. In this mode the analyzer stores "profiles" of the data stored in the memory along both zero axes of the two-parameter spectrum. (The zero axes values are not profiles in the strict sense of the word since the zero-channel data are actually the sum of the data in all channels having the same ADC address.)

The above procedures served to calibrate the complete system electronically. The test input to the system was at the preamplifier and the observed output was recorded in the multichannel analyzer memory. The next step was to test the system response to neutron sources.

The detector bias was set to 2100 volts and a well moderated PuBe neutron source was positioned adjacent to the detector. Data were accumulated until the thermal peak began to appear in the spectrum. The pulse height channel amplifier gain was adjusted to place the 0.764-MeV thermal neutron peak in channel 25. The thermal neutron pulse risetime was determined by noting the channel in the risetime spectrum where the peak occurred. With the risetime spectrum

digitized into 16 slices the peak appeared in slice number 5 corresponding to a risetime of about 2.5 microseconds.

Figure 16 shows a plot of the thermal neutron plus pulse generator spectrum along both the risetime and pulse height axes for a pulse generator setting of 5 microseconds and 5 volts. It was observed that selection of the third risetime slice, for example, yields a thermal neutron peak attenuation of 0.035. Thus risetime can be used to discriminate against the thermal neutron contribution to the spectrum. In the pulse height spectrum the thermal neutron resolution at full-width-half-maximum (FWHM) is seen to be about 33 keV.

Next, the spectrometer system response was checked using a Chicago Nuclear, 9500 series, neutron generator as a neutron source. The reaction used to produce neutrons is the  $d(d,^3He)n$  reaction which has a Q-value of 3.27 MeV. The neutron generator accelerates deuterons through a potential of 150 kV to strike a deuterium-titanium target which is thick enough to absorb the deuteron beam. The energy of the neutrons produced under such conditions is a function of the angle of the emitted neutrons with respect to the incident beam, the maximum energy occurring when the angle is zero and the minimum occurring when the angle is  $180^\circ$ . Seagrave (31) shows that the maximum neutron energy emitted is 2.85 MeV and that when the emission angle is small (i.e.  $< 15^\circ$ ) there is less than 1% energy deviation over the subtended solid angle.

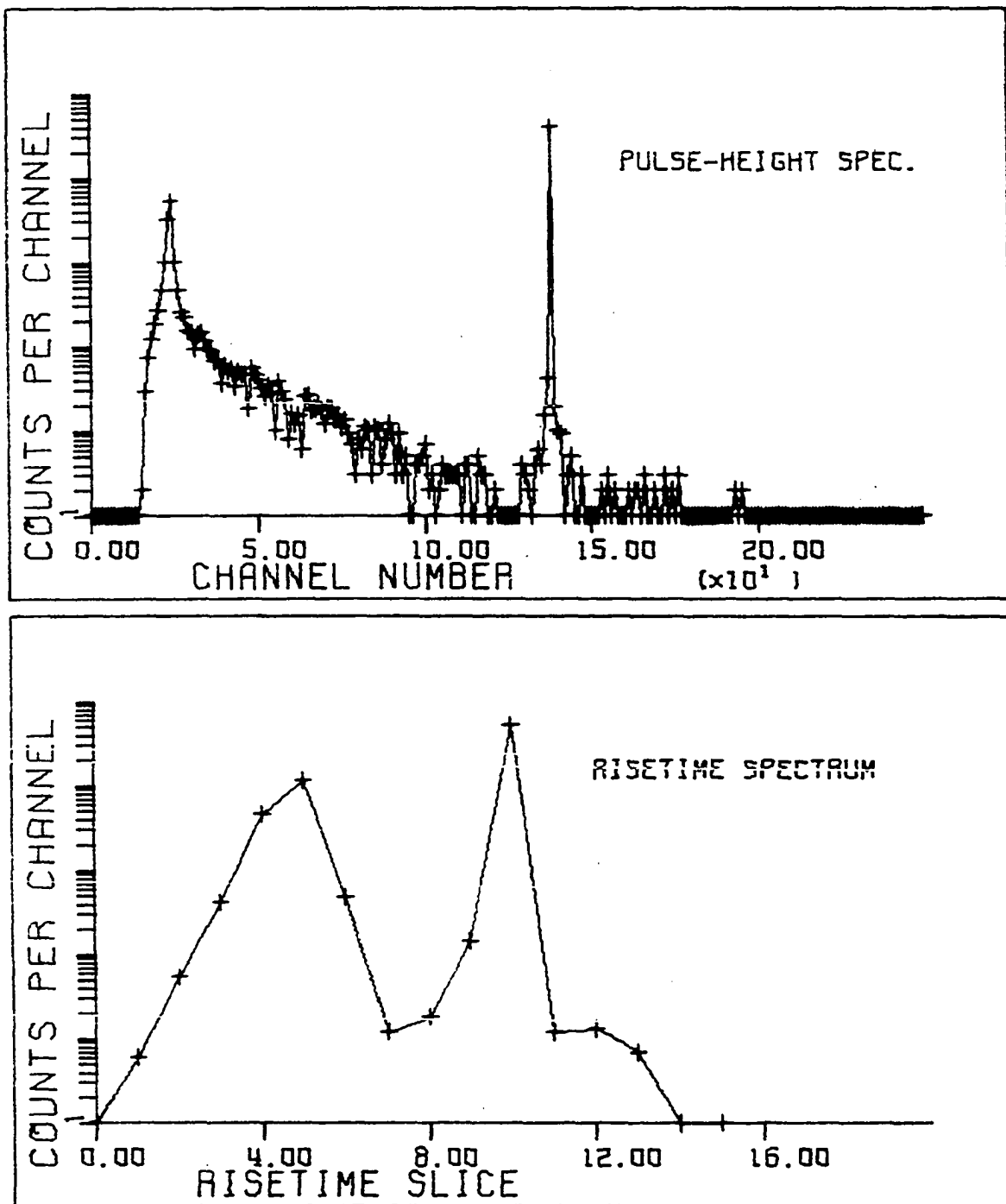


Figure 16. Pulse height and risetime response  
for thermal neutrons

Therefore, if the active volume of a  $^3\text{He}$  proportional counter is included within the above solid angle the counter will be exposed to a monoenergetic neutron source of 2.85 MeV.

When a  $^3\text{He}$  proportional counter is exposed to monoenergetic neutrons of energy  $E = 2.85 \text{ MeV}$ , the full-energy peak in the pulse height spectrum will be equivalent to  $E + Q$ , or  $3.614 \text{ MeV}$ . Furthermore, the maximum energy neutrons in the recoil distribution will occur at a pulse height of  $0.75E$ , or  $2.137 \text{ MeV}$ . Finally, the thermal neutron peak will occur at a pulse height equivalent to  $0.764 \text{ MeV}$ . Thus, three calibration points can be determined by observing the spectrum of 2.85-MeV neutrons.

When performing the measurements the  $^3\text{He}$  detector was covered with both gamma and thermal neutron shields and placed in a room background shield box. The background shield consists of a cubical box, 16 inches on a side and was constructed from 0.25-inch boral. A 3-inch diameter hole was cut in the center of one face of the box to expose the detector to the neutron source. The background shield containing the detector and preamplifier were positioned near the neutron generator target and a steel collimator 10 inches in length was placed between the target and detector. The collimator consists of a 3-inch outside diameter steel rod with a tapered hole along the axis having a 1-inch diameter

at the source end and a 1.5-inch diameter at the end adjacent to the detector. The collimator and background shield box were used to shield the detector from all neutrons except those within a small cone about the incident beam. The spectrometer system was tested for proper calibration with the precision pulser and a thermal neutron source. Finally, the detector high voltage was allowed to stabilize while the neutron generator was placed in operation. With the neutron generator operating at about 200 microamperes of beam current a neutron count rate of about 300 counts per second was observed. A 6000-second, two-parameter pulse height analysis run was taken and position of the full-energy peak and maximum of the recoil distribution were recorded. The full-energy peak was observed in pulse height channel 180 with a FWHM resolution of about 315 keV or about 9.4%. The maximum recoil energy was observed to occur in channel 95 and the thermal neutron peak was observed in channel 25. Figure 17 shows a plot of the observed energies versus channel numbers and the resulting linear calibration curve. The calibration curve was compared with the known energies of  $^{17}\text{N}$  delayed neutrons which were used as a final calibration test for the spectrometer system.

The  $^{17}\text{N}$  delayed neutrons were produced by irradiating a sample of enriched lithium nitride ( $^6\text{Li}_3^{15}\text{N}$ ) in the R-8 pneumatic tube facility of the Ames Laboratory Research

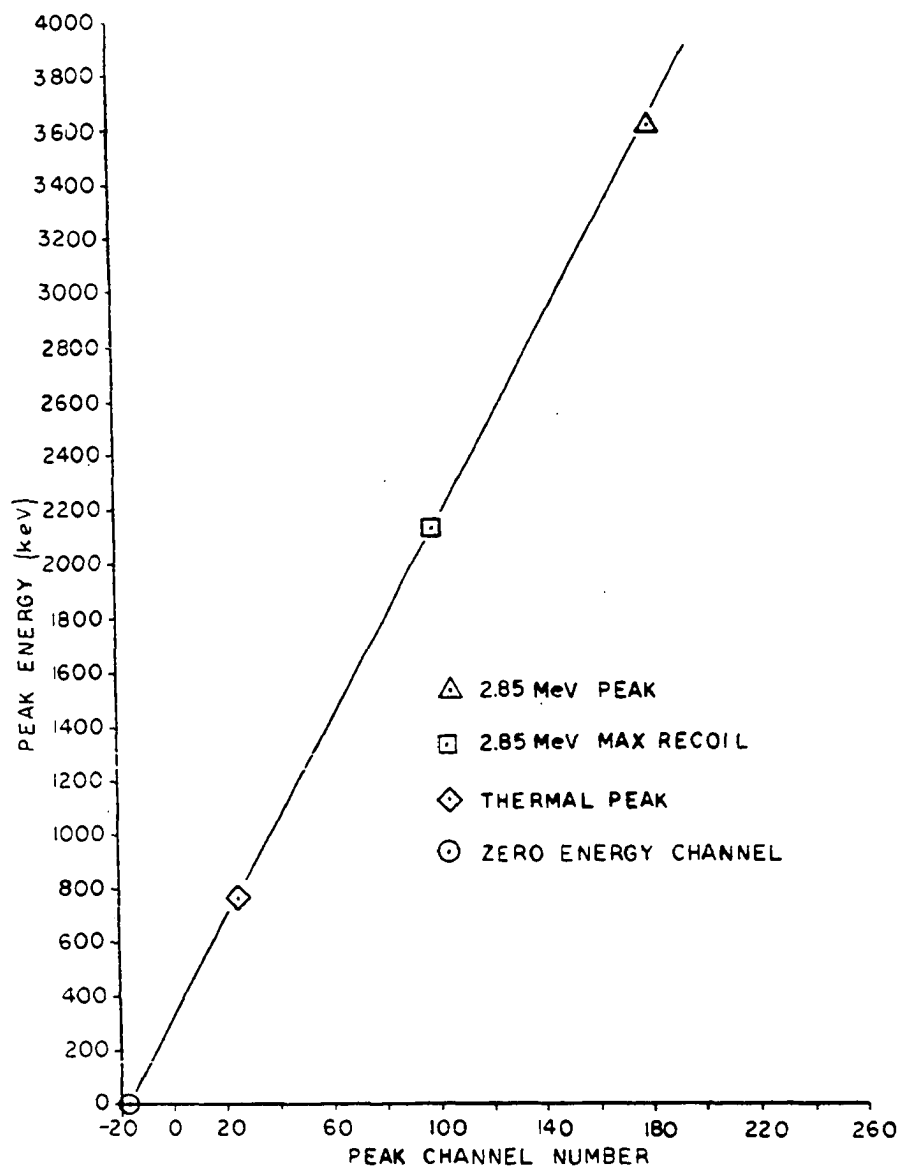


Figure 17.  ${}^3\text{He}$  proportional counter energy calibration

Reactor. The sample was enriched to 99.3% in both isotopes and was in the form of light grey amorphous crystals. The neutron producing reaction is initiated by thermal neutron absorption of the  $^{6}\text{Li}$  to produce tritons via the  $^{6}\text{Li}(\text{n},\text{T})^{3}\text{He}$  reaction. The emitted tritons can then interact with the  $^{15}\text{N}$  atom to produce  $^{17}\text{N}$  via the  $^{15}\text{N}(\text{T},\text{p})^{17}\text{N}$  reaction. Finally, the  $^{17}\text{N}$  beta decays with a 4.1-second half-life to neutron emitting levels in  $^{17}\text{O}$ .

The sample was contained in a specially prepared polyethylene capsule which was mounted in a polyethylene support frame and enclosed in a standard large rabbit capsule. Several 0.125-inch diameter holes were drilled in each end of the rabbit capsule to allow the pneumatic system transport air to flow over the sample capsule during irradiation and provide forced cooling for the lithium nitride.

The R-8 pneumatic irradiation facility terminates in a heavily shielded room in the reactor basement used as a counting room. The pneumatic transfer system was arranged to move the rabbit capsule from the receiver in the counting room to the reactor where it was irradiated for a selected period of time. At the end of the irradiation time the rabbit capsule was automatically returned to the receiver which held the capsule in a reproducible position during the neutron counting period. At the end of the preselected counting period the sample was automatically recycled until

sufficient counting statistics were obtained. The rabbit receiver was arranged to accommodate either the long counter or the  $^3\text{He}$  proportional counter complete with its background shield box.

The total travel distance from the rabbit receiver to the irradiation location within the reactor is about 85 feet. The minimum transit time which could be tolerated for continuous cycling without damage to the polyethylene rabbit capsule was 7 seconds. Because of the relatively short half-life of  $^{17}\text{N}$  a 20- to 25-second irradiation was sufficient to obtain effective activity saturation. Thus, a typical cycle required 60 seconds; 7 seconds transit time to the reactor, 26 seconds irradiation time, 7 seconds transit time from the reactor to the rabbit receiver, and 20 seconds of data collection.

Previous work by Sher and Floyd (32) reported the yield of  $^{17}\text{N}$  per gram of ordinary lithium nitride when irradiated in the Brookhaven National Laboratory reactor at a location where the thermal neutron flux was  $10^{13}$ . Since the thermal neutron flux in the R-8 facility of the ALLR is also approximately  $10^{13}$  it was necessary only to correct for the isotopic enrichment in order to estimate the yield of  $^{17}\text{N}$  per gram of enriched lithium nitride. Using the known efficiency of the long counter, the transit time, and the irradiation time the expected long counter count rate at the end of irradiation of

a 20-milligram sample was calculated to be  $1.53 \times 10^4$  counts per second. A 20.5-milligram sample was then loaded into the sample irradiation capsule and inserted into the pneumatic tube. The long counter was positioned at the rabbit receiver in its proper position and a single sample irradiation cycle was initiated. The long counter output was connected to a multichannel analyzer operating in the time multiscale mode which was automatically started by the arrival of the sample at the rabbit receiver. The multiscale data was taken so that the neutron activity half-life could be measured in order to verify that the delayed neutron activity was due to  $^{17}\text{N}$ . A quick estimate of the half-life from the multichannel analyzer display yielded a value of 4.3 seconds which was in good agreement to the expected value. Furthermore, the time multiscale data was extrapolated back to the end of the sample irradiation time for comparison with the calculated yield and found to be  $1.68 \times 10^4$  counts per second. This was in excellent agreement with the calculated value above.

Next, an efficiency comparison was made between the long counter and the  $^3\text{He}$  spectrometer using  $^{17}\text{N}$  delayed neutrons. First, the efficiency of the long counter was calibrated for the rabbit system counting geometry by alternately placing a PuBe and an AmLi source in the pneumatic tube at the counting position and recording the count rate for each. The long counter efficiency was observed to be 2.25%. Then, the lith-

ium nitride sample was placed in the pneumatic tube and five cycles were run with the total counts over the 20-second counting cycle recorded for each run. Finally, the long counter was removed and the  $^3\text{He}$  spectrometer was positioned at the counting position. Again, several cycles were run with the lithium nitride and the total counts over the 20-second counting cycle were recorded. The procedure yielded a counting efficiency of 0.0043% for the  $^3\text{He}$  spectrometer. Because of the low  $^3\text{He}$  spectrometer efficiency the lithium nitride sample weight was increased to 0.25 gms for all spectrometer runs.

With the  $^{17}\text{N}$  source strength determined and the  $^3\text{He}$  spectrometer in place at the rabbit receiver counting position the multichannel analyzer was placed in the two-parameter plus profile mode and a new lithium nitride sample was installed in the pneumatic tube. The sample irradiation cycle was initiated and continued for eight hours. A plot of a typical two-parameter calibration run is shown on Figure 18.

Observation of the two-parameter spectrum revealed three obvious peaks in addition to the thermal neutron peak in channel 25. The peaks appeared at channels 44, 87, and 116. Using the calibration curve of Figure 17 the peaks should correspond to neutron energies of 376, 1166, and 1694 keV respectively. These values are quite close to the recently re-

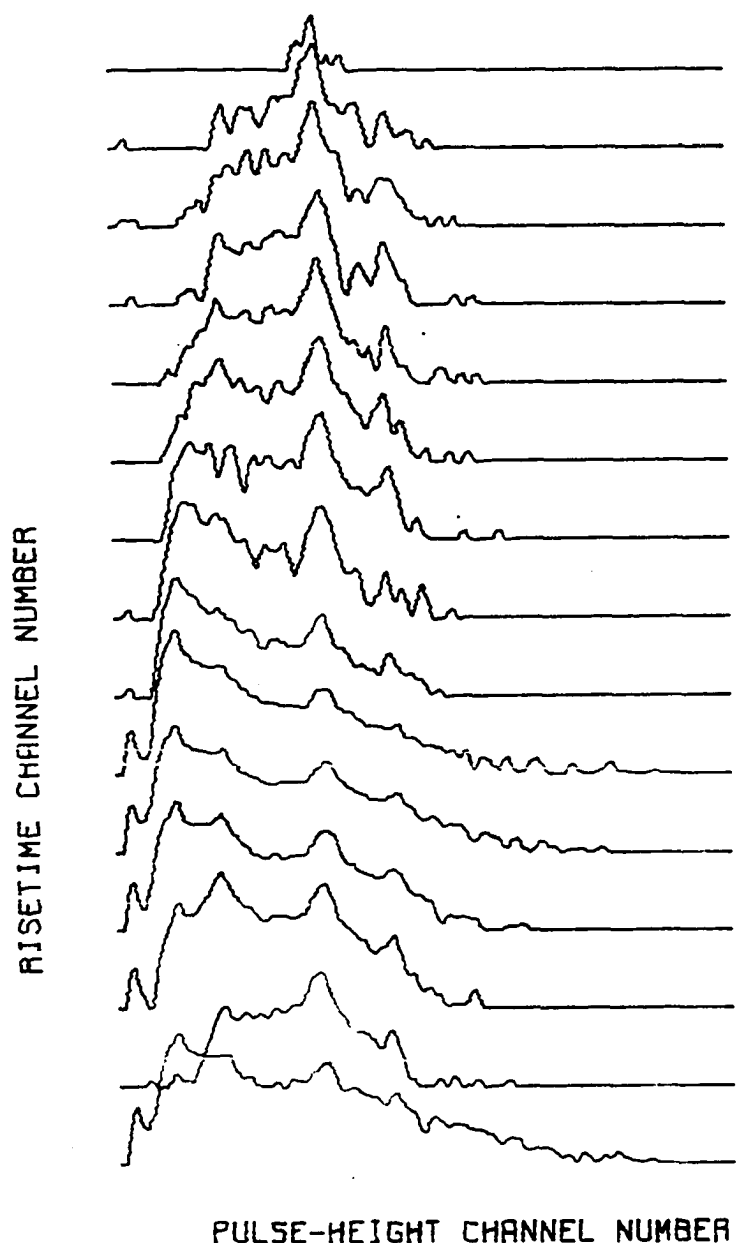


Figure 18. Typical two-parameter  $^{17}\text{N}$  spectrum

ported measurements by Shalev (33) of  $387 \pm 5$ ,  $1170 \pm 10$ , and  $1678 \pm 10$  keV respectively for the three neutron peaks in the decay of  $^{17}\text{N}$ . Since the  $^{17}\text{N}$  data was used as a calibration, the Shalev data were assumed to be correct and the peak channel values were plotted at the Shalev energy values along with the data presented on Figure 17 to yield a final calibration curve. Figure 19 is a plot of each of the calibration points and the linear least square fit to the data for the final calibration curve of the  $^3\text{He}$  proportional counter spectrometer system.

Selected rise time slice plots of the  $^{17}\text{N}$  data are presented under results and discussion.

## 2. $^3\text{He}$ ionization chamber

The  $^3\text{He}$  ionization chamber used for this study was purchased from the Technion Research and Development Foundation. The detector was one of the early production models of the detector developed by Shalev (33) and Cuttler *et al.* (34).

The detector consists of a cylindrical cathode, axial anode, axial grid assembly, and integral gas purifier. The active volume of the detector is 2 inches in diameter and 6 inches in length. The detector filling gas consists of 6 atmospheres  $^3\text{He}$ , 3 atmospheres Ar, and 0.45 atmospheres methane.

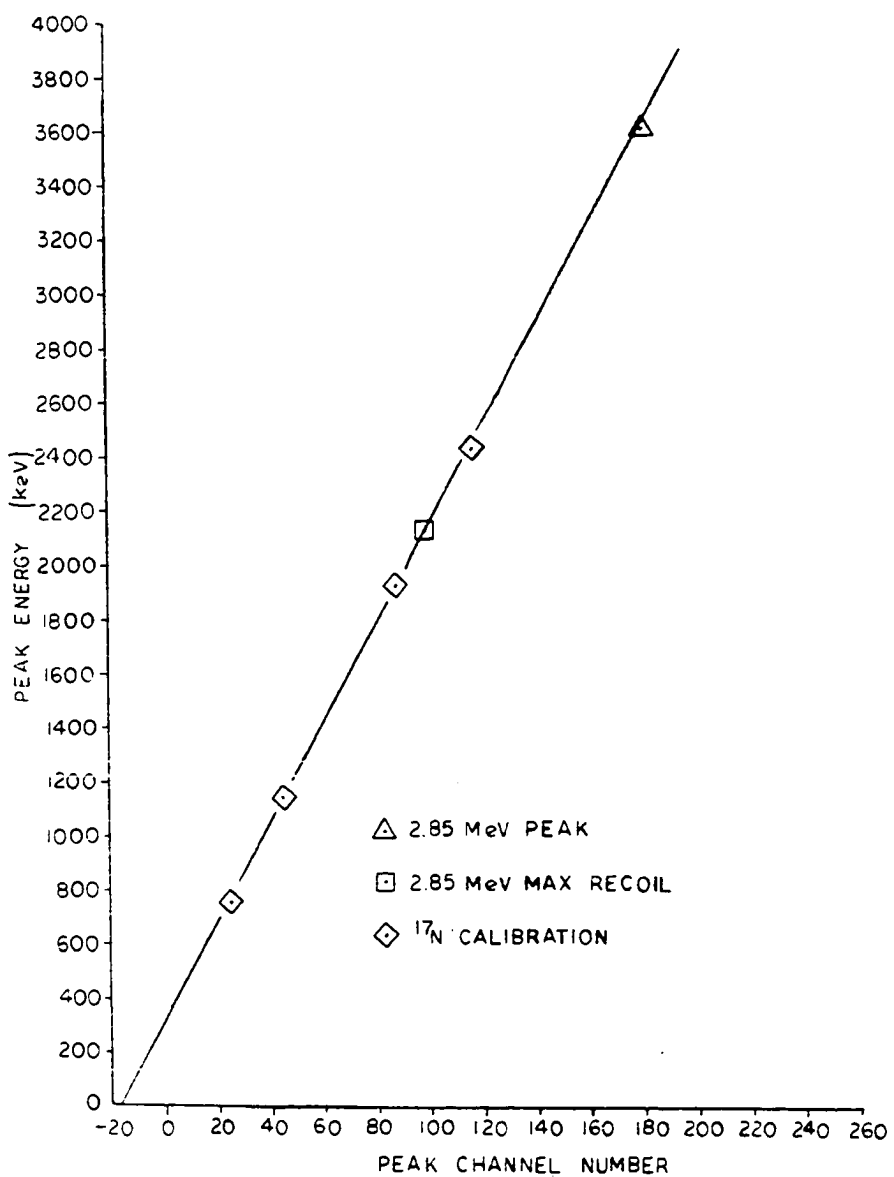


Figure 19. Final  ${}^3\text{He}$  proportional counter calibration

The purchase specifications required resolution of the thermal neutron peak to be less than 20 keV FWHM and the 1-MeV neutron peak to be less than 40 keV FWHM. Also included in the purchase price were detector calibration and response function measurements with thermal, 200-, 400-, 700-, 1000-, 1300-, and 1600-keV neutrons.

The calibration procedure for the detector involved initial setup and check out of the detector, testing the thermal neutron response and resolution, and measuring the energy spectrum of  $^{17}\text{N}$  to verify the manufacturer-supplied calibration data.

Prior to initial detector testing, a cadmium thermal neutron shield, a Pb gamma shield, and a boral room background shield were fabricated and fitted to the detector. The thermal neutron shield was made from 0.030-inch cadmium sheet and wrapped tightly around the active detector region. Additional cadmium cans were prepared to enclose the detector ends and fittings. The gamma shield was fabricated from a single ingot of Pb by boring a 2.25-inch diameter hole along the axis and cutting along the vertical center line with a bandsaw. The background shield was constructed with 0.25-inch boral sheet using plans supplied by the manufacturer. A 3-inch diameter hole was cut in one face of the background shield to expose the detector to neutron sources. The base of the background shield was equipped with

special shock absorbing legs to minimize mechanical vibration transmission to the detector.

Figure 20 shows three photographs of the detector shields during assembly. The upper picture shows the detector with the cadmium shield around the active region and the integral gas purifier with heating tapes and thermocouple leads. The center picture shows the cadmium shielded detector mounted in the background shield box with two faces removed. The lower photograph shows the completed detector assembly.

The electronics setup used during initial detector testing is shown in Figure 21. Since the detector is a guided ionization chamber two bias voltages are required; one for the anode and one for the grid. The anode power supply was set at +5000 volts and the grid power supply was set at +1200 volts as recommended by the manufacturer. Both power supplies were equipped with high frequency noise filters on the high voltage output which served to reduce noise transmission to the detector via the high voltage power supplies.

The preamplifier was attached directly to the detector signal output connector and its output fed to the main amplifier which was then connected to the input of the multichannel analyzer ADC. The stabilizer units shown on the figure were a later addition to the system and were not used

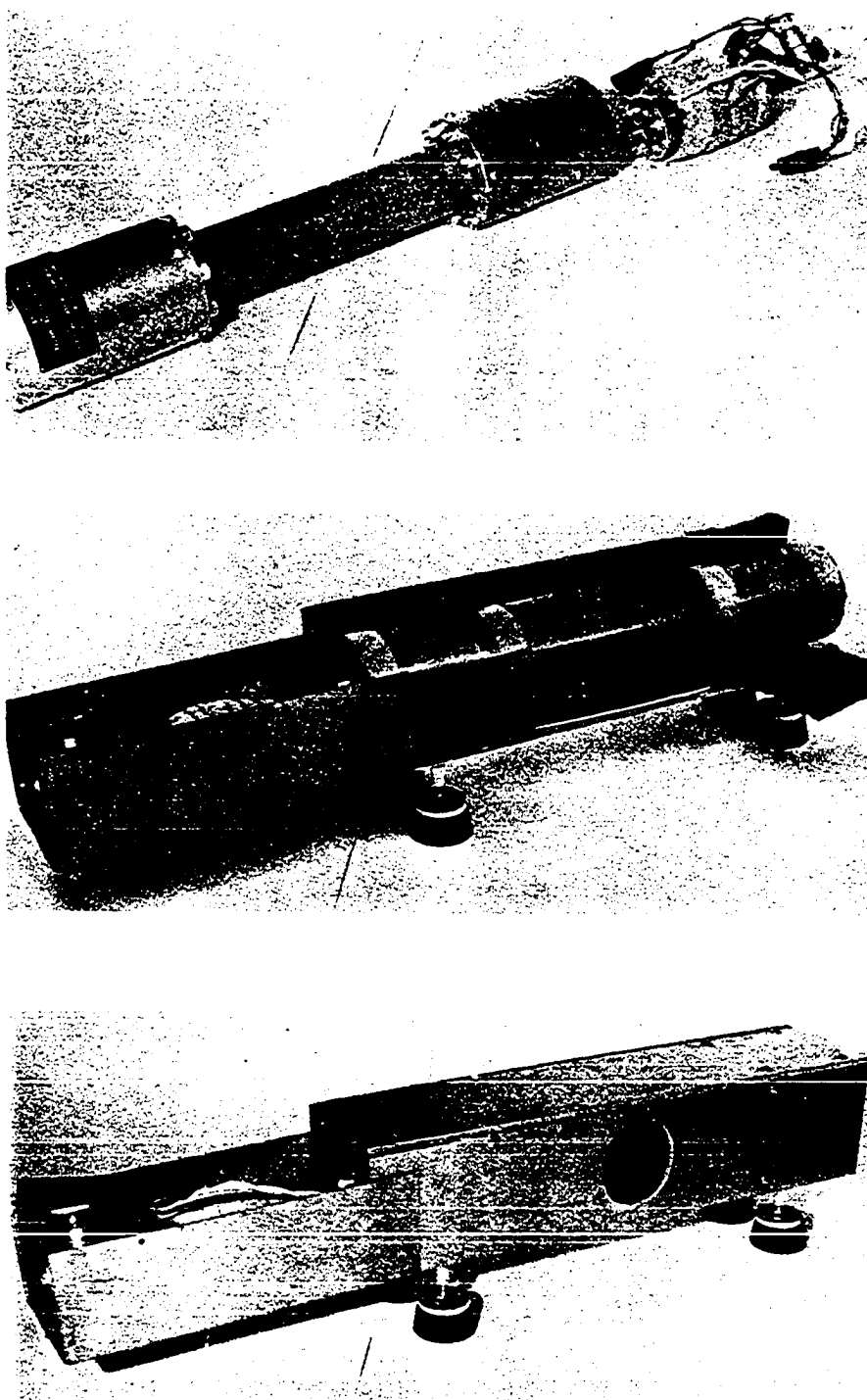


Figure 20.  $^3\text{He}$  ionization chamber shield configuration

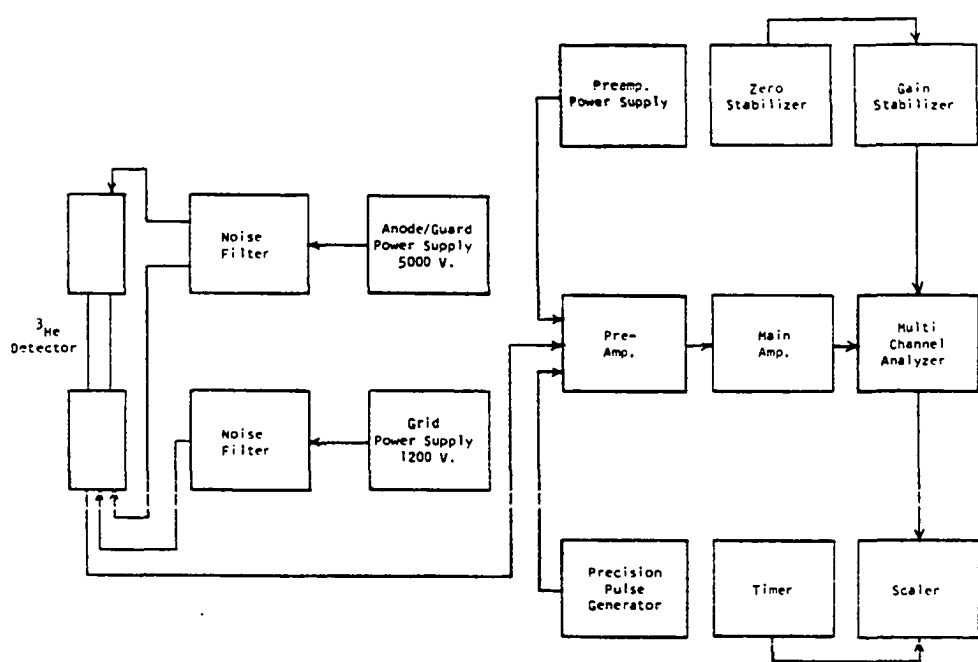


Figure 21. Schematic of  ${}^3\text{He}$  ionization chamber electronics

for initial detector testing. However, when incorporated in the system the function of the stabilizers was to provide automatic gain shift correction. One of the stabilizers was set to monitor the thermal neutron peak and correct the system zero and the other was set to monitor the pulser peak and adjust the overall system gain. The precision pulser was set at a pulse height near the upper end of the spectrum. The pulser ran continuously and was recorded with every spectrum to yield a quantitative measure of the system pulse height resolution capability.

Initial system testing with the voltages set to their proper values and the pulser generating a peak in the pulse-height spectrum showed the spectrometer to be ultra sensitive to audible noise and mechanical vibration. After a great deal of trial and error a mechanical damping arrangement was discovered which greatly reduced the sensitivity to vibration. The detector with its shock absorbing feet was mounted on two Pb bricks which in turn rested on a 0.375-inch thick plywood plate of dimension 8 inches by 20 inches. The plywood plate was supported by a layer of rubberized horse hair packing material which then rested directly on the steel top of the movable detector stand. The arrangement was successful in eliminating the transmission of mechanical vibration to the detector for all cases except direct blows to the background shield, preamplifier case, or high voltage cables.

The microphonic or audible noise sensitivity was reduced to acceptable levels by operating the system main amplifier in the automatic baseline restoration (BLR) mode. The BLR mode of operation assumes the amplifier output pulse to consist only of a symmetric positive lobe (i.e. a unipolar pulse) so that when the falling portion of the positive lobe reaches the baseline the output is maintained at the baseline until another pulse arrives for processing. The effect is to reduce amplifier output oscillation due to microphonic noise on the preamplifier signal. However, loud audible noise sources such as alarms, slamming airlock doors, paging system operation, etc. could not be successfully filtered and some noise invariably was present in the pulse height spectrum.

The system pulse height response characteristics were checked using a precision pulser which was fed to the test input of the preamplifier. The pulser amplitude was adjusted so that the peak appeared in channel 751. The pulser amplitude attenuation switches were then used to generate pulse heights equal to 0.5, 0.2, and 0.1 times the initial pulse height. A linear least squares curve fit through the points resulted in a -12.2-channel zero-energy intercept for the system.

Next, a well moderated PuBe source was used to test the thermal neutron response of the detector. The multichannel analyzer was placed in the pulse height analysis mode and set

for a 1024-channel spectrum. The system gain was adjusted to place the thermal neutron peak in the middle of the spectrum and the pulser peak near the upper end of the spectrum. An eight-hour accumulation was taken from which the thermal neutron peak resolution was observed to be 18.8 keV FWHM. The system gain was adjusted to place the thermal neutron peak in channel 152 of the 1024 channel spectrum for a calibration of about 5 keV per channel.

The detector response to  $^{17}\text{N}$  delayed neutrons was measured using the same techniques as described for the  $^3\text{He}$  proportional counter. A new rabbit sample was prepared containing 0.27 grams of enriched lithium nitride and placed in the pneumatic tube. The detector was moved to the rabbit receiver and placed in the counting position. The system was set to accumulate in a 1024-channel spectrum and several manual cycles of the rabbit sample were made to check the count rate and spectrometer response. The runs revealed that the buildup of gamma background radiation in the sample seriously degraded the spectrometer resolution. Additional Pb shielding was positioned around the rabbit receiver such that a total of 10 centimeters of Pb was interposed between the rabbit sample in the receiver and the detector.

The primary source of gamma radiation in the sample was caused by neutron absorption in  $^{15}\text{N}$  leading to  $^{16}\text{N}$ . The  $^{16}\text{N}$  beta decays with a 7.2-second half-life to excited levels of

$^{160}$  which depopulate with the emission of a number of gammas having energies above 6 MeV. Thus, the gamma radiation could not be removed at the source. However, because of the gamma level of the source it served as a good model of fission product delayed neutron emission since in all cases delayed neutron emission from fission products is accompanied by a fairly large gamma background.

A final  $^{17}\text{N}$  delayed neutron run was made with the 10-centimeter Pb shielding in place. The data run was followed by a background run for the same length of time. The three peaks in the  $^{17}\text{N}$  spectra appeared at channels 227, 400, and 516 which were plotted at 387, 1170, and 1678 respectively to yield the calibration curve of Figure 22. The background corrected spectrum for  $^{17}\text{N}$  in using the  $^3\text{He}$  ionization chamber is presented under results and discussion.

### 3. Comparative effeciency of the spectrometer systems

A final test of both spectrometers was made to determine the comparative efficiency and the effect of the improved resolution of the ionization chamber on the comparative thermal peak height.

Both detectors were set up on a laboratory workbench and positioned symmetrically with respect to a well moderated PuBe neutron source such that each detector intercepted the same solid angle of source neutrons.

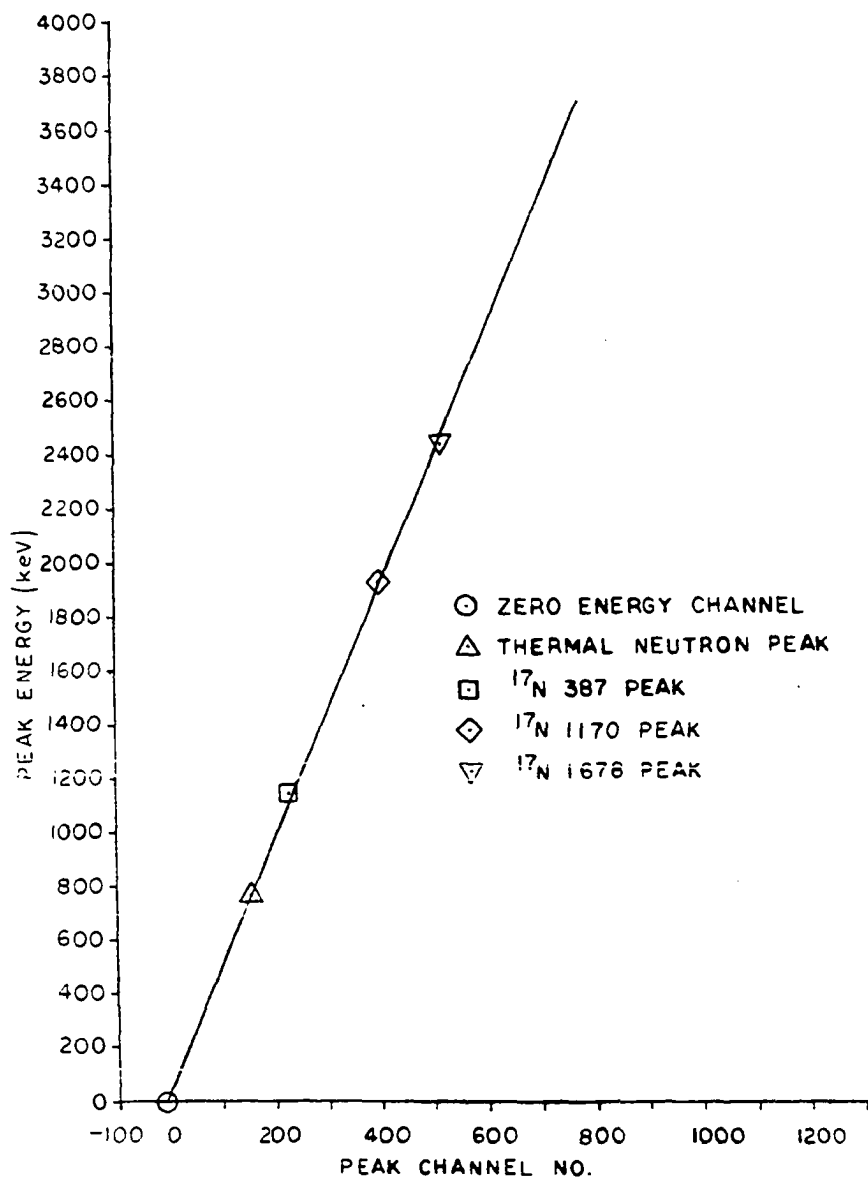


Figure 22.  $^3\text{He}$  ionization chamber energy calibration

Two simultaneous 2048-channel spectra were collected for a sufficient length of time to accumulate about 1000 counts in the thermal peak of the proportional counter.

The thermal neutron count rate of the ionization chamber was observed to be 49% greater than the proportional counter, in good agreement with the ratio of  $^3\text{He}$  gas filling in the detector. The thermal peak resolution of the ionization chamber for the run was 19.4 keV compared to 39.4 keV for the proportional counter.

Comparison of the thermal peak height of the two detectors yielded a value of 3.05 for the ratio of the ionization chamber peak to the proportional counter peak. This was in good agreement with the efficiency ratio times the inverse FWHM ratio for the two detectors.

## IV. RESULTS AND DISCUSSION

## A. Half-life Measurements

A total of five delayed neutron precursor half-life measurements were made using the time multiscale measurement technique described earlier. The multiscaling conditions for each mass are given in Table 2. The observed multiscale data and the fitted half-life components are shown for each measured mass in Figures 23-27.

The primary purpose of the runs was to measure the half-lives of the halogen fission product precursors. The halogen fission product activity was made available for study by the use of the uranyl stearate fission product source described in Chapter III. The stearate, however, also served as a source of hydrogen due to break down of the stearate components under thermal neutron and gamma irradiation. The hydrogen then was available to form hydride compounds with the fission products either in the fission product generator or the mass separator ion source.

The so-called "hydride contamination" resulted in two parent nuclides, normally separated by one mass unit, being present in the mass separator beam at the activity deposit point. For example, the neutron multiscale data for mass 137 shown in Figure 23 contained some fraction of  $^{136}\text{I}$  activity

Table 2. Neutron multiscaling conditions

Mass	Analyzer Settings (sec/ch.)	Collect Time (no. of chs.)	Decay Time (sec)	Count Time (sec)
137	4	99	100	300
138	2	100	30	170
88	4	64	64	192
89	1	144	20	125
93	0.4	252	30	95
				101

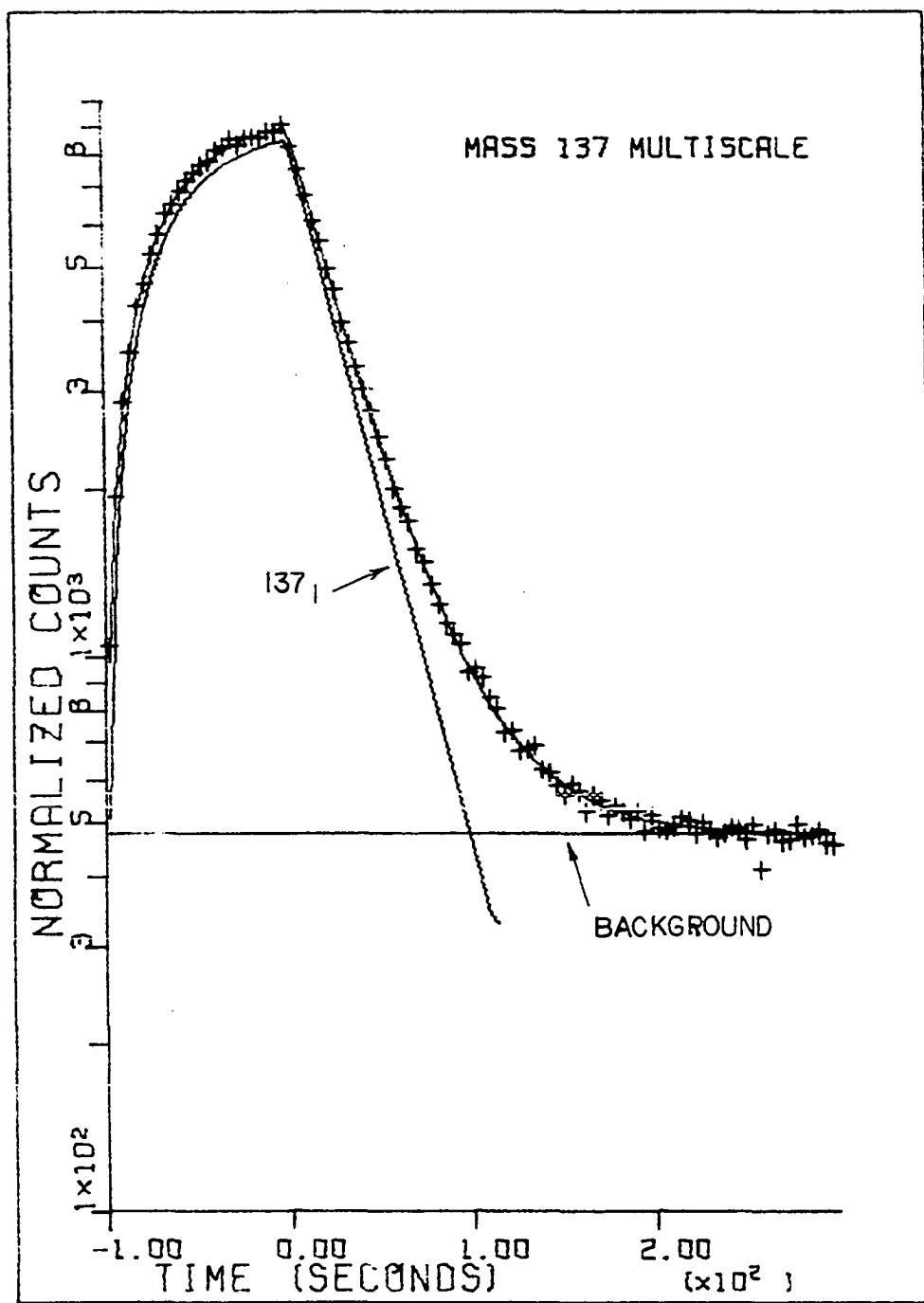


Figure 23. Decay of neutron activity for mass 137

deposited as  $^{136}\text{IH}^+$ . However, the neutron multiscale data shows only one component since neither  $^{136}\text{I}$  or its stable daughter are delayed neutron precursors and  $^{137}\text{I}$  is the only precursor in the mass 137 decay chain.

The multiscale data for  $A=138$  shown in Figure 24 demonstrates the effect of hydride contamination. The presence of the  $^{137}\text{IH}^+$  component in the decay curve is evident. Since it was desired to obtain the best fit value for the half-life of  $^{138}\text{I}$ , the measured value of the half-life of  $^{137}\text{I}$  from the previous run was used for the half-life of the  $^{137}\text{IH}^+$  component. Thus the decay curve was analyzed by fixing the value of the hydride component half-life and allowing the background level and the  $^{138}\text{I}$  half-life to vary until the best data fit was obtained.

A slightly different situation existed for the analysis of the neutron decay of mass 88 shown in Figure 25. For this case the hydride contamination component was due to  $^{87}\text{Br}$  which was not measured in this study due to low counting rate. Thus the half-life used in the decay curve fitting program for the  $^{87}\text{BrH}^+$  component was the adopted value of 55.7 seconds (35). With the hydride contribution half-life fixed, the background and  $^{88}\text{Br}$  half-life were adjusted to obtain the best fit to the data.

The same technique was used for the mass 89 multiscale data shown in Figure 26. The half-life obtained for  $^{89}\text{Br}$  in

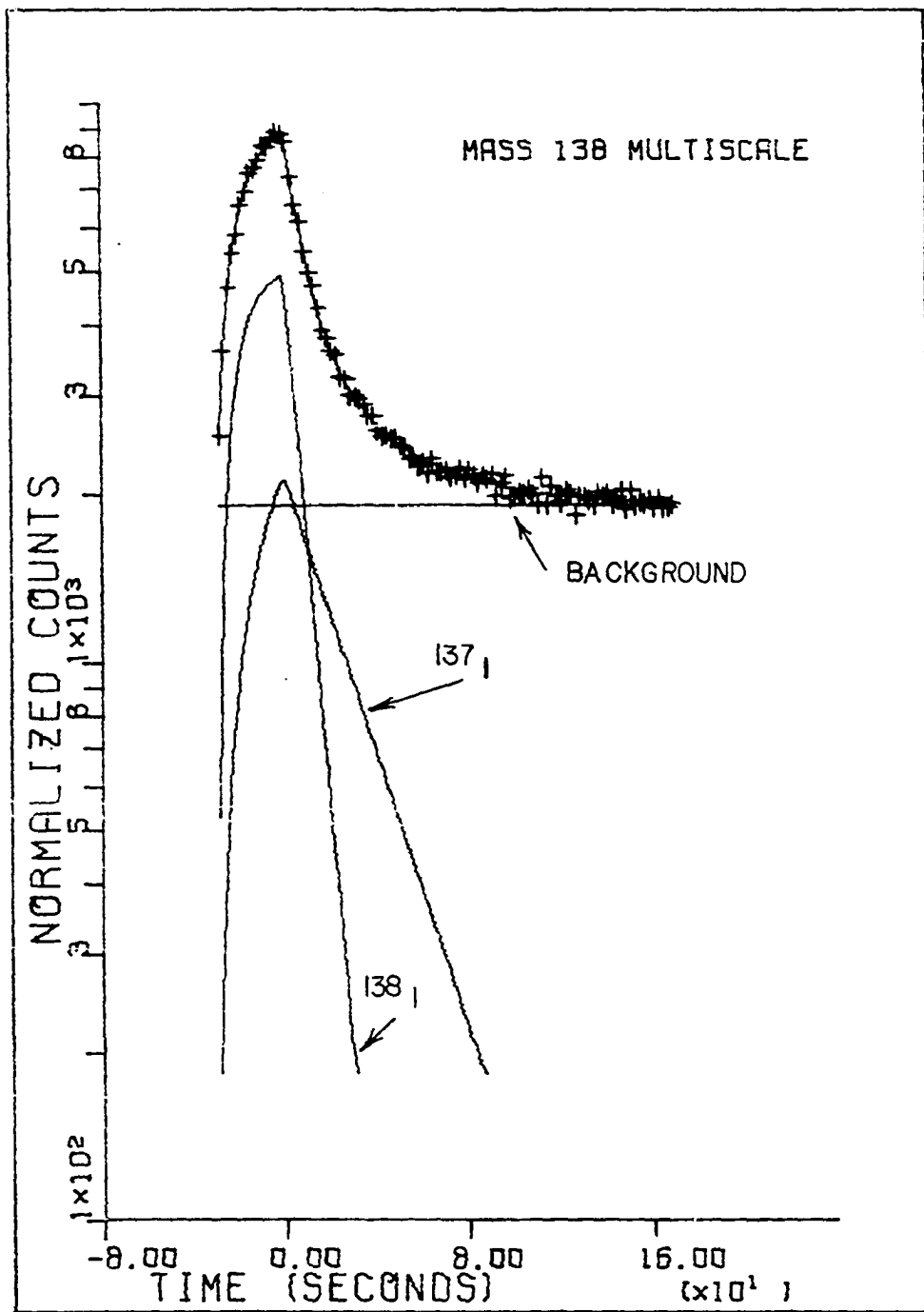


Figure 24. Decay of neutron activity for mass 138

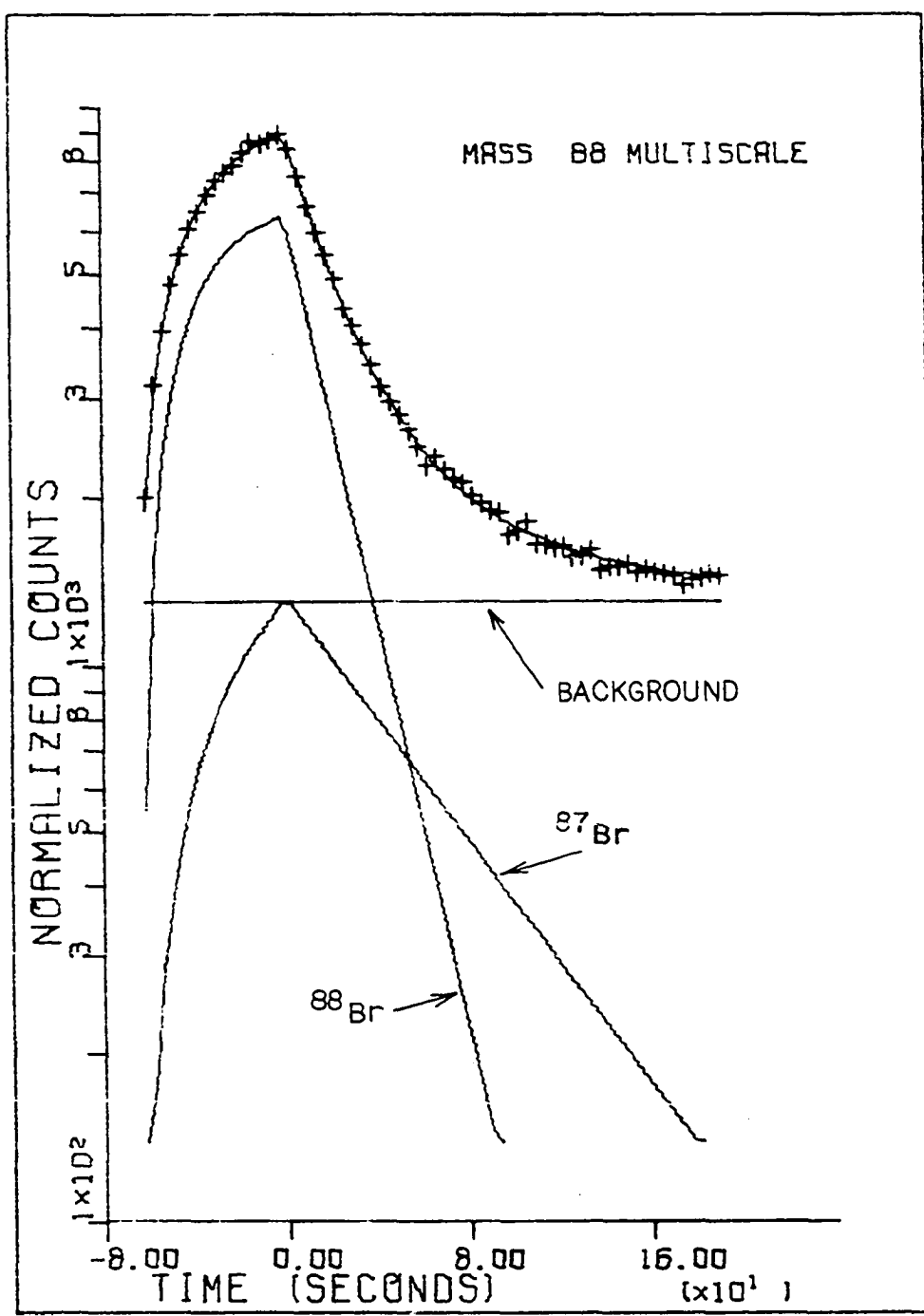


Figure 25. Decay of neutron activity for mass 88

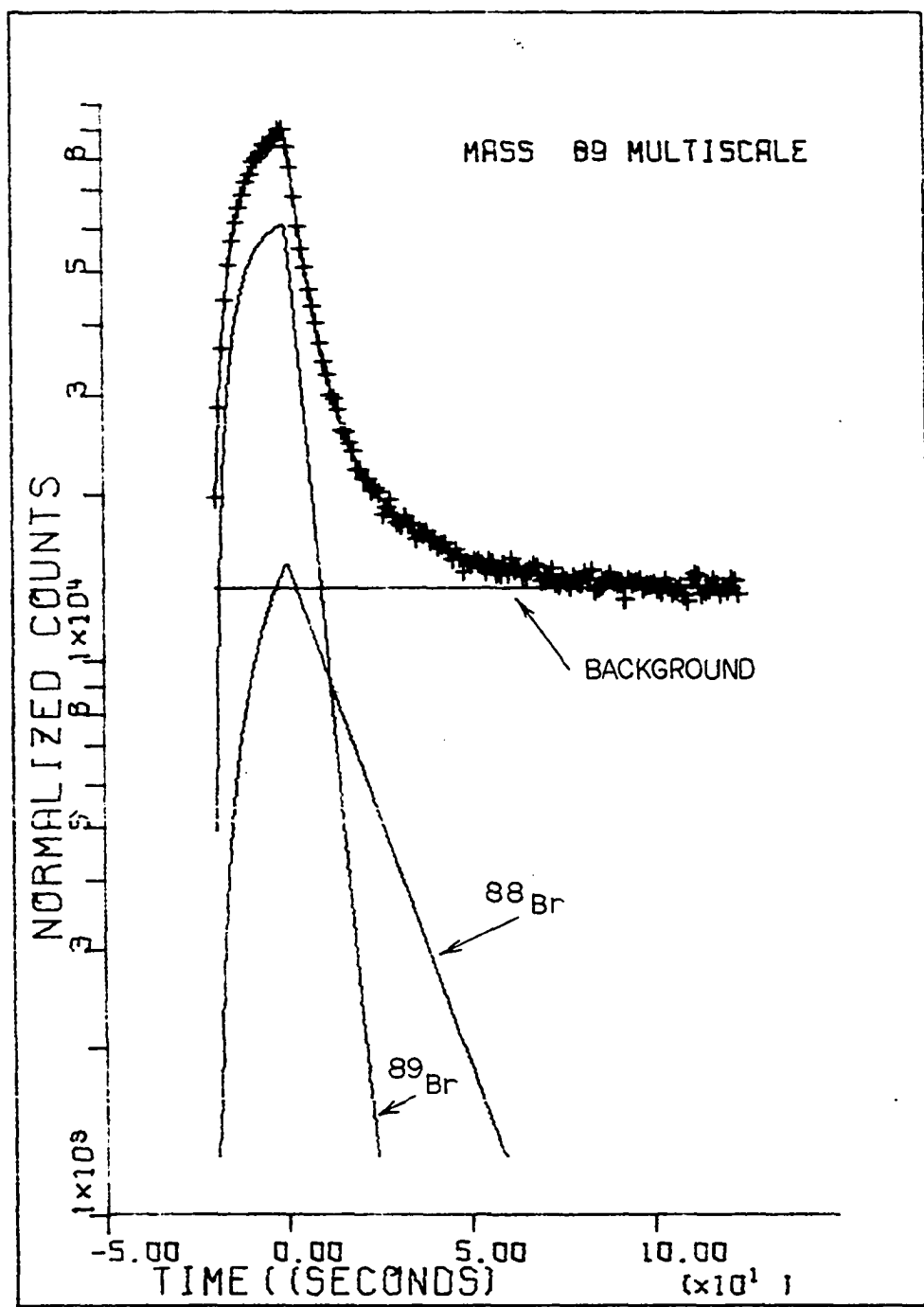


Figure 26. Decay of neutron activity for mass 89

the mass 88 multiscale run was held fixed for the hydride contribution and the background and  $^{89}\text{Br}$  half-life were adjusted to obtain the best fit to the data.

The hydride formation appeared to be limited to the halogen fission products as evidenced by the mass 93 multiscale run shown in Figure 27. The neutron multiscale data for mass 93 appears to contain only the  $^{93}\text{Kr}$ -parent and  $^{93}\text{Rb}$ -daughter activity and shows no evidence of  $^{92}\text{Kr}$ -parent or  $^{92}\text{Rb}$ -daughter activity. Due to the low neutron emission probability values for these  $A=92$  precursors (12), however, this absence of such activities is not surprising. Also, the mass 93 decay components show the characteristic parent-daughter relationship as contrasted with the two-component decay curves for masses 88, 89, and 138.

The results of the half-life measurements are summarized in Table 3. The mean value reported by Tomlinson (8) is the average of the reported measurements available for each nuclide. The agreement with the mean value is acceptable for most cases and essentially verifies previously used half-life measurements.

#### B. Neutron Spectrum Measurements

A summary of the neutron spectrum measurements made in this study is presented in Table 4. A total of five different neutron spectra were measured using various combinations

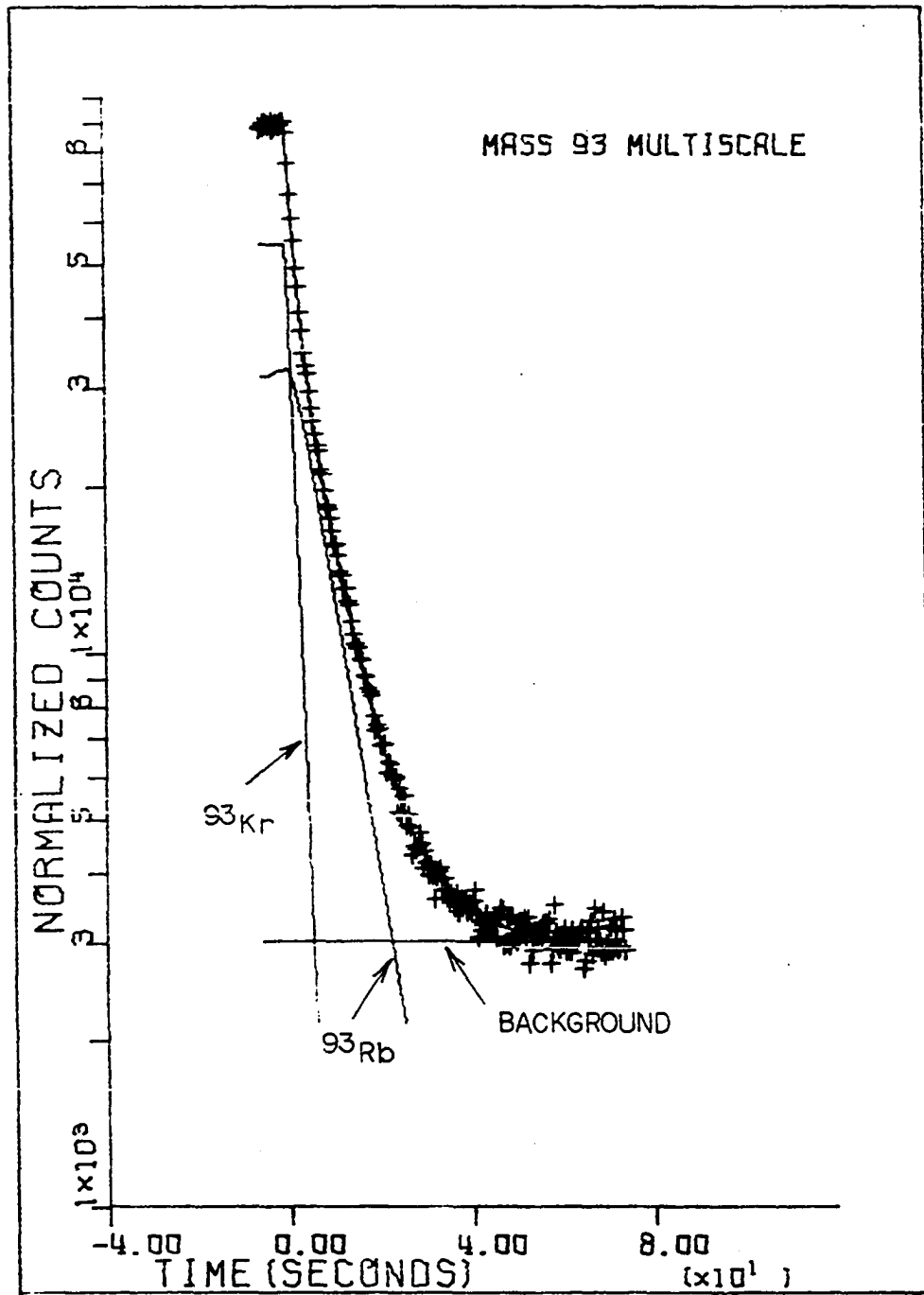


Figure 27. Decay of neutron activity for mass 93

Table 3. Half-life measurement results

Mass	Nuclide	Activity Type	Measured Half-life (sec)	Mean Value* (sec)
137	$^{137}\text{I}$	Parent	24.42 $\pm$ .08	24.62 $\pm$ .08
138	$^{138}\text{I}$	Parent	6.40 $\pm$ .17	6.55 $\pm$ .11
88	$^{88}\text{Br}$	Parent	16.52 $\pm$ .34	15.88 $\pm$ .11
89	$^{89}\text{Br}$	Parent	4.32 $\pm$ .05	4.55 $\pm$ .09
93	$^{93}\text{Kr}$	Parent	1.296 $\pm$ .022	1.287 $\pm$ .016
93	$^{93}\text{Rb}$	Daughter	5.926 $\pm$ .044	5.86 $\pm$ .12

\* L. Tomlinson (8)

Table 4. Summary of spectrum measurements

Spectrum Measured	$^3\text{He}$ Proportional Counter	$^3\text{He}$ Ionization Counter
$^{17}\text{N}$	Yes	Yes
$^{137}\text{I}$	Yes	No
$^{93}\text{Kr}$ & $^{93}\text{Rb}$ in equilibrium	Yes	Yes
$^{93}\text{Kr}$ enhanced	No	Yes
$^{93}\text{Rb}$ enhanced	No	Yes

of the two neutron spectrometers.

With the exception of  $^{17}\text{N}$  which was used for calibration purposes, the choice of which spectrometer to use for each spectrum measurement was dictated by the experimental equipment and fission product activity available at the time of the measurement. For example, during the period of time that the fission product generator (FPG) was producing abundant quantities of  $^{137}\text{I}$ , the  $^3\text{He}$  proportional counter was the only spectrometer that was on hand. After the  $^3\text{He}$  ionization chamber had been received and calibrated, the emanation properties of the FPG had changed and halogen fission products were no longer produced in quantities large enough for study. Attention was then focused on the noble gas fission products and mass 93 was selected for study since the A=93 decay chain had the largest neutron activity. The delayed neutron spectrum of  $^{93}\text{Kr}$  and  $^{93}\text{Rb}$  in equilibrium was measured with both spectrometers and the results are compared. Finally, the  $^3\text{He}$  ionization chamber was used in conjunction with a moving tape collector at the activity deposit point to separate the parent and daughter activities of the A=93 decay chain using the techniques described in Appendix A.

The first delayed neutron spectrum measurements made with each of the spectrometers were taken using the  $^{17}\text{N}$  activity as a calibration source. Table 5 gives a summary of the peak energy observed for the three prominent neutron

Table 5.  $^{17}\text{N}$  delayed neutron spectrum energies

Peak Number	Shalev's Data* (keV)	$^3\text{He}$ Proportional Counter (keV)	$^3\text{He}$ Ionization Counter (keV)
1	387 ± 5	376	346
2	1170 ± 10	1166	1161
3	1678 ± 10	1694	1706

\* Shalev (33)

peaks in the decays of  $^{17}\text{N}$  and compares the values with the reported values of Shalev (33). The listed energy values for the  $^3\text{He}$  proportional counter and the  $^3\text{He}$  ionization chamber were determined by selecting the peak channel number for each peak in the spectrum and referring to the appropriate energy calibration curve to determine the associated energy.

A comparison of the  $^{17}\text{N}$  neutron spectra measured in this study and the reported spectrum of Shalev (33) is shown in Figure 28. The upper curve shows the spectrum measured with the  $^3\text{He}$  proportional counter using risetime discrimination. The middle curve shows the  $^{17}\text{N}$  spectrum measured with the  $^3\text{He}$  ionization chamber under the same experimental conditions, while the lower curve is the referenced measurement. The lower spectrum was measured with the same type of detector as was the middle spectrum except that the source of  $^{17}\text{N}$  was different. The referenced spectrum was obtained by thermal neutron irradiation of  $^6\text{Li}_2\text{C}^{18}\text{O}_3$ , to initiate the  $^6\text{Li}(\text{n},^4\text{He})\text{T}$  reaction followed by the  $^{18}\text{O}(\text{T},^4\text{He})^{17}\text{N}$  reaction to produce  $^{17}\text{N}$ .

From Figure 28 it is clear that the raw spectra measured with both the  $^3\text{He}$  proportional counter and the  $^3\text{He}$  ionization chamber compare favorably with the referenced spectrum in peak energy placement. With regard to spectrum shape, peak width, and relative peak height, it is also obvious that the  $^3\text{He}$  proportional counter using risetime discrimination is

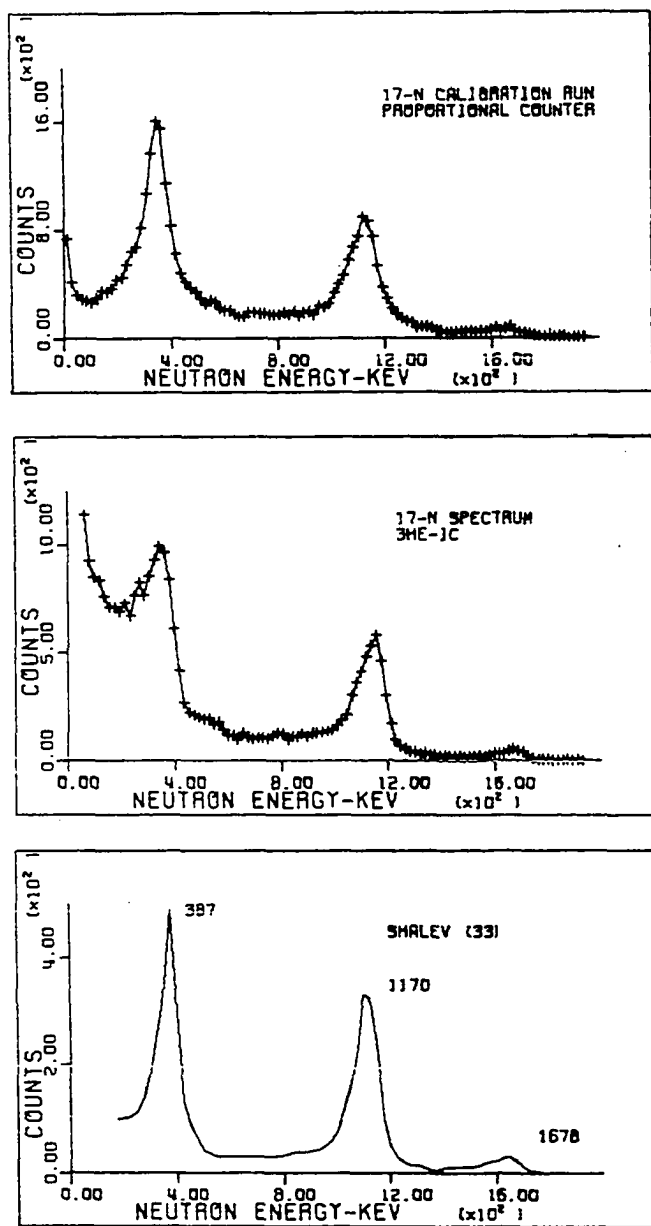


Figure 28. Comparative  $^{17}\text{N}$  spectra

superior to the  $^3\text{He}$  ionization chamber. The spectrum measured with the  $^3\text{He}$  proportional counter is the sum of all pulses originating in the detector having risetimes in the range 1.0 to 1.5 microseconds which corresponds to the sum of the pulse height information in risetime slices number 2 and 3 of the two-parameter spectrum.

The risetime range was selected to discriminate against the thermal neutron peak, the wall effect and recoil pulses, and the gamma induced pulse distribution. The peak of the thermal neutron distribution occurred at about 2.5 microseconds in the pulse height spectrum and was thus greatly suppressed by eliminating these pulses with risetimes greater than 1.5 microseconds. Since the wall effect pulses exhibit a broad distribution of risetimes above the thermal peak risetime, the selected risetime cutoff greatly reduced the recoil distribution contribution to the spectrum. The recoil neutron distribution is characterized by risetimes shorter than 1.0 microseconds. The effectiveness of the discrimination system for recoil events can be observed from the spectrum. A recoil distribution accompanies both the 1170 keV and 1678 keV peaks and the maxima of the recoil distributions should appear at about 880 keV and 1260 keV, respectively. The measured spectrum shows no evidence of distributions ending at those energies. Finally, the gamma induced events originating in the detector were rejected by gating

the multichannel analyzer off for all pulses which were below the threshold setting of the pulse shape analyzer in the risetime discrimination channel.

The raw spectrum obtained with the  $^3\text{He}$  ionization chamber as shown in Figure 28 exhibits rather poorer characteristics than that selected using the  $^3\text{He}$  proportional counter. One reason for the poorer quality of this spectrometer involves the extremely high gamma-ray activity level of the  $^{17}\text{N}$  source due to thermal neutron activation of the  $^{15}\text{N}$  in the sample to produce  $^{16}\text{N}$  activity. The high-energy gamma emission following the beta decay of  $^{16}\text{N}$ , coupled with the strong gamma sensitivity of the detector, produced undesirable pulse pile-up on the high-energy side of the peaks. The most troublesome pile-up occurs on the high-energy side of the thermal neutron peak because the pile-up pulse distribution extends well into the region of interest for delayed neutron spectrum measurements. The energy peaks in the spectrum are therefore superimposed on a sloping pulse pile-up distribution which in the case of small peaks can wash out the details of the spectrum. The gamma pile-up observed in the spectrum occurred even though there was nearly 10-cm of Pb between the  $^{17}\text{N}$  source and the detector. The addition of more gamma shielding would have reduced the neutron detection efficiency below the point that was considered acceptable for studying the rather low neutron activity levels

available from isotope separator system.

The attempt to use risetime discrimination for this detector failed because of a singularly undesirable feature of the ionization chamber type detector; namely, its microphonic sensitivity. It would appear that vibrations transmitted to the grid assembly within the detector either from mechanical motion or interaction with audible sound waves is responsible for the poor signal quality. It was not possible to isolate the detector sufficiently to reduce the noise to a level low enough to allow successful risetime analysis of the pulses.

The marked difference between the two lower spectra which were measured using essentially identical detectors and similar electronic systems can perhaps be explained by the differences in the methods of producing  $^{17}\text{N}$ . It is possible that the thermal neutron activation of the components in the  $^6\text{Li}_2\text{C}^{18}\text{O}_3$  sample yields much less gamma background than does the  $^6\text{Li}_3^{15}\text{N}$ . It is certain that the gamma energies would be less for the carbonate than for the nitride compound. Furthermore, if the relative gamma level provides the proper explanation for the differences in the  $^{17}\text{N}$  spectra, since all cases of fission product delayed neutron emission are expected to be accompanied by a large gamma background, the most useful neutron spectrometer must be relatively insensitive to such background.

It should also be noted that the response function measurements of the  $^3\text{He}$  ionization chamber provided by the manufacturer were made in an essentially gamma free environment. However, the response of the detector in an environment of various gamma energies or a combined gamma plus neutron environment is not known. Therefore, it is difficult if not impossible to use spectrum unfolding techniques based on neutron response functions for gamma contaminated spectra.

The first fission product delayed neutron spectrum measured in this study was that of  $^{137}\text{I}$ . The  $^3\text{He}$  proportional counter spectrometer was used for the measurement and the risetime discrimination system settings were the same as for the  $^{17}\text{N}$  spectrum measurement above. Since the mass 137 delayed neutron activity consisted of only a single component, the isotope separator was set to continuously deposit mass 137 at the neutron counting point and the  $^{137}\text{I}$  delayed neutron activity was measured under equilibrium conditions. Data were collected continuously for about 67-hours. Table 6 gives a summary of the observed peak energies in the spectrum. The listed energy values for the peaks were obtained by selecting the peak channel of the pulse height distribution for each peak and using the measured energy calibration curve to determine the energy.

Figure 29 shows a comparison of the measured spectrum for  $^{137}\text{I}$  and that reported by Shalev and Rudstam (36). The

**Table 6.**  $^{137}\text{I}$  delayed neutron spectrum energies

Prominent Peak Number	Shalev's Data* (keV)	$^3\text{He}$ Proportional Counter (keV)
1	270	260
2	380	375
3	488	490
4	570	570
5	756	750
6	863	825
7	965	950
8	1140	1115
9		1330

\* Shalev and Rudstam (36)

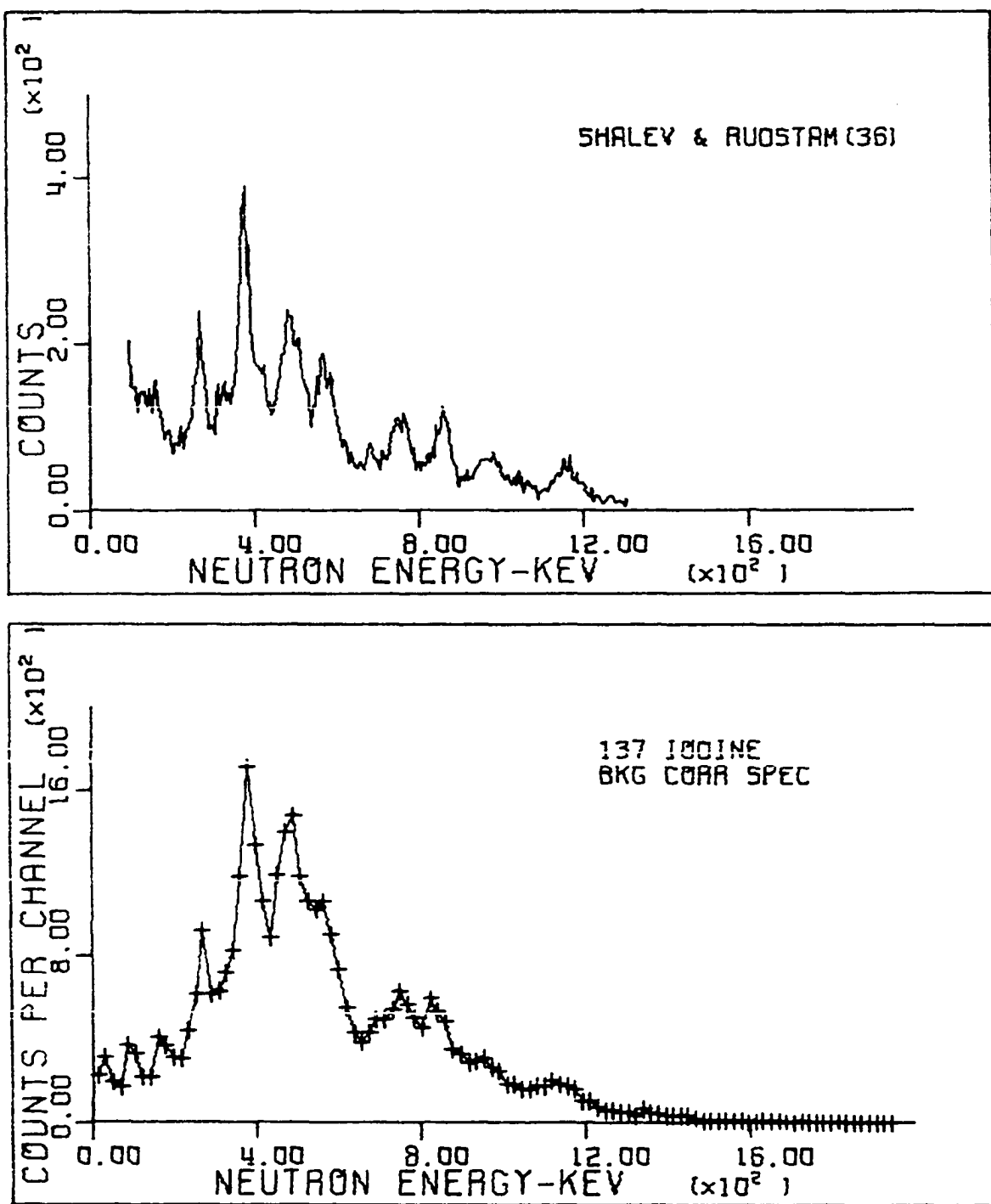


Figure 29. Comparative  $^{137}\text{I}$  spectra

spectra are in excellent agreement when it is recognized that the energy resolution of the  ${}^3\text{He}$  ionization chamber used for the referenced spectrum is approximately a factor of two better than the  ${}^3\text{He}$  proportional counter used for this study. Although no error values are quoted for the referenced spectrum, the agreement between the two measurements is good to within 15 keV for all except the 863-keV and the 1140-keV peaks of the referenced spectrum. Also, this study shows that an additional peak may be present at 1330 keV; however, the number of counts in the peak are quite small and additional data would be required to establish its existence with certainty.

It should be noted further that whereas in the  ${}^{137}\text{I}$  spectrum there is an obvious difference in the width of the peaks in the two spectra due to differences in resolution of the two spectrometers, such is not the case for the  ${}^{17}\text{N}$  spectrum. This would indicate that the neutron-emitting states in  ${}^{17}\text{O}$  are contained in three separated but diffuse groups while the neutron-emitting states of  ${}^{137}\text{Xe}$  are more localized.

With the  ${}^3\text{He}$  proportional counter spectrometer performance verified by measuring spectra for both  ${}^{17}\text{N}$  and  ${}^{137}\text{I}$  delayed neutrons, measurements were begun to characterize the neutron emission spectrum for the mass 93 fission products. It is well known that both Kr and Rb are delayed neutron

precursors in the A=93 decay chain. The first measurements made were for the case of equilibrium counting conditions for both parent and daughter activities. Both spectrometer systems were used to obtain equilibrium spectra. First, a 50-hour run was made using the  ${}^3\text{He}$  proportional counter with the same risetime electronics settings as before. Then a 35-hour run was made using the  ${}^3\text{He}$  ionization chamber spectrometer under slightly different counting conditions. For the proportional counter run, the mass separator beam was allowed to continuously deposit activity at the neutron counting point, and  ${}^{93}\text{Kr}$  and  ${}^{93}\text{Rb}$  were counted in equilibrium with the rest of the decay chain. However, due to the gamma sensitivity of the  ${}^3\text{He}$  ionization chamber the activity for this run was deposited on the movable tape of a moving tape collector (MTC) so that the gamma activity build up of the longer-lived members of the decay chain could be moved away from the detector periodically. The counting conditions and MTC operation required to accomplish the gamma activity removal are covered in Appendix A.

Table 7 gives a listing of the apparent energy peaks in the mass 93 equilibrium spectrum as measured by both spectrometers. The peak energies were determined, in the case of the  ${}^3\text{He}$  proportional counter, by selecting the peak channel number and using the energy calibration curve to obtain the energy at the peak. The values obtained for the  ${}^3\text{He}$  ioniza-

Table 7. Delayed neutron spectrum energies of  $^{93}\text{Kr}$   
 $^{93}\text{Rb}$  in equilibrium

Peak Number	$^3\text{He}$ Proportional Counter (keV)	$^3\text{He}$ Ionization Counter (keV)
1	140	137
2	233	230
3	306	304
4	343	-
5	398	-
6	435	451
7	656	-

tion chamber tend to verify the results of the  $^3\text{He}$  proportional counter. Figure 30 shows the spectra obtained using the two spectrometers. The uncertainty in the determination of the peak energy values for the  $^3\text{He}$  ionization chamber is obvious. However, it is apparent that the irregularities superimposed on the gamma distribution above the thermal peak in the case of the  $^3\text{He}$  ionization chamber are in direct correspondence with some of the peaks observed in the  $^3\text{He}$  proportional counter spectrum.

A final series of runs was made using the MTC techniques described in Appendix A. The purpose of these runs was to separate the Kr and Rb activity in order to determine what differences might exist in the spectra of the two and perhaps identify which peaks in the equilibrium spectra were associated with each nuclide. Figure 31 shows the results of the Kr-enhanced and Rb-enhanced spectra. The Kr-enhanced spectrum consisted of about 87% Kr activity and 13% Rb activity. The Rb-enhanced spectrum consisted of about 7% Kr and 93% Rb activity.

The Kr-enhanced spectrum is quite similar to the previous equilibrium run shown in Figure 30. The most striking feature of the Rb-enhanced spectrum is the almost total lack of structure. While there is some indication of structure in the region of 200-400 keV, it is not possible to make any identification due to the poor resolution of the detector.

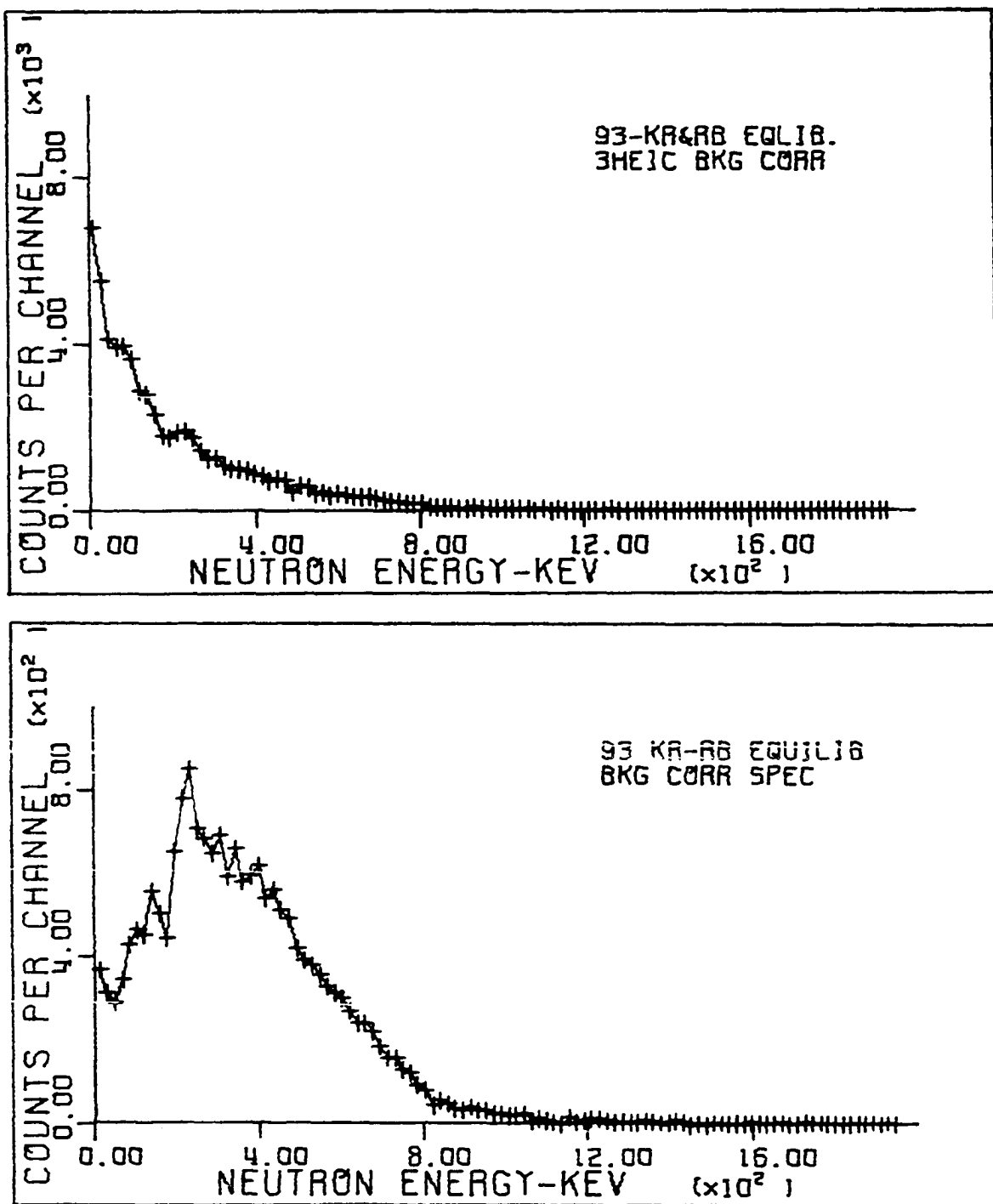


Figure 30. Comparative mass 93 spectra

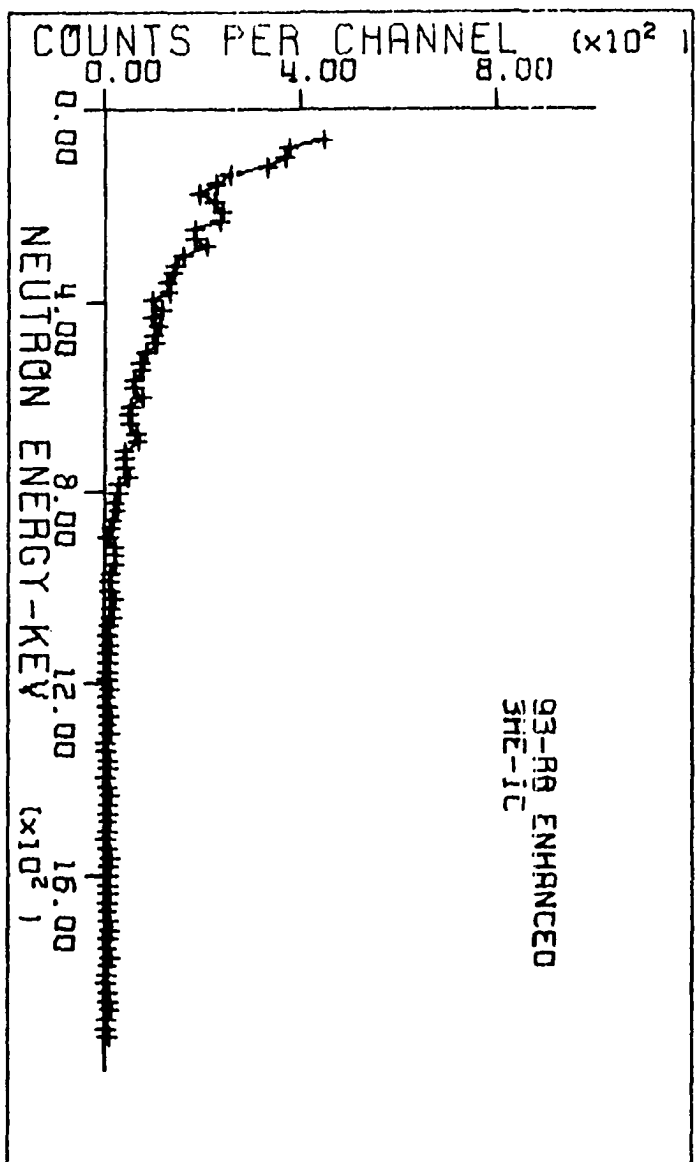


Figure 31.  $^{93}\text{Kr}$  and  $^{93}\text{Rb}$  spectra

## V. CONCLUSIONS

The results of this study have demonstrated the efficacy of an on-line isotope separator for the study of mass-separated fission product delayed neutron precursors. Furthermore, the use of a moving tape collector at the activity deposit point can provide enhancement of the activity of the nuclide of interest in the decay chain of the deposited mass. Thus an on-line isotope separator with a moving tape collector at the activity deposit point provides a unique arrangement for the detailed study of any fission product or its subsequent decay products, provided the fission product can be removed from the fission source and transported to the ion source of the isotope separator.

The general agreement of the half-life measurements with adopted values verifies that on-line identification of individual delayed neutron precursors can be made with certainty. However, since neutron multiscaling can be done easily in the presence of high gamma backgrounds, the results of such measurements not only provide identification of the precursor but also serve as an independent check of the beta-decay half-life of the precursor. The result of the neutron multiscaling half-life measurement of  $^{93}\text{Kr}$  is an example of the excellent agreement with the beta-decay half-life determination. The mean value quoted for this half-life was based

primarily on the highly accurate measurement reported by Carlson et al. (37) in which several gamma transitions following the beta-decay of  $^{93}\text{Kr}$  were individually multiscaled and the results averaged.

Due to the high counting rate observed at mass 93 in this study, it is possible that the half-life measurement for  $^{93}\text{Rb}$  is an improvement over the mean value since the uncertainty for this measurement is considerably smaller.

The half-life measurement of  $^{137}\text{I}$  is a case in which a highly accurate determination was made both due to a high neutron counting rate for the nuclide and the lack of competing activities in the decay. However, the value obtained is smaller than the reported mean value. Among the reported measurements of the half-life of  $^{137}\text{I}$  the results of Perlow and Stehney (38) are closely corroborated by this study with a factor of five improvement in the uncertainty over their results.

The high precision available for measuring precursor half-lives using the neutron multiscaling technique is evidenced by the low uncertainty limits obtained even under non-optimum conditions. For example, the equilibrium neutron activity at mass 138 was the lowest of the nuclides measured. However, for  $^{138}\text{I}$  the uncertainty obtained was only about 2.7% of the measured value and the measurement is in good agreement with the mean half-life value for this nuclide.

The values obtained for the half-lives of  $^{88}\text{Br}$  and  $^{89}\text{Br}$  are somewhat dependent upon the value of the half-life for  $^{87}\text{Br}$  which appeared in  $^{88}\text{Br}$  multiscaling data due to hydride contamination. Since the bromine half-lives monotonically decrease with increasing mass number above mass 87, it would appear that if the  $^{87}\text{Br}$  half-life value used in the fitting program was either too large or too small, a systematic error would be indicated in the results obtained for  $^{88}\text{Br}$  and  $^{89}\text{Br}$ . Such was not the case. The measured value of  $^{88}\text{Br}$  was significantly larger than the mean value and the measured value of  $^{89}\text{Br}$  was smaller than the mean value. Here it should be noted that these measurements agree more closely with the reported values of Perlow and Stehney (38) for these nuclides than with the mean values.

In summary, it is obvious that neutron multiscaling techniques can be used for the measurement of beta-decay half-lives to a high degree of accuracy. It is unlikely that further refinements of the half-life determinations for these nuclides will be necessary for reactor kinetics calculations.

The comparison between measured spectra and reported spectra for both  $^{17}\text{N}$  and  $^{137}\text{I}$  delayed neutrons using the  $^3\text{He}$  proportional counter with risetime discrimination was used as a test of the spectrometer system. The excellent agreement obtained lends confidence to the spectra observed for mass 93

for which no comparative spectra exist.

Since delayed neutrons are emitted from levels in the emitter nuclide above the neutron binding energy, the observation of well-defined peaks in the delayed neutron energy spectrum can be used to calculate the energies of neutron-emitting states in the emitter nuclide. However, the observation of a smooth distribution of neutron energies in the emission spectrum would suggest that a large number of neutron-emitting states exist in the emitter nuclide. Such information can be used to calculate level densities and/or level widths at high excitation energies and to provide additional input for theoretical developments that may lead to a better understanding of nuclear forces.

The obvious differences in the spectra of  $^{137}\text{I}$ ,  $^{93}\text{Kr}$  and  $^{93}\text{Rb}$  indicate that no general features of delayed neutron spectra can be concluded at this time. The rather sharply peaked spectrum of  $^{137}\text{I}$  is in stark contrast to the apparently smooth distribution of neutron energies emitted by  $^{93}\text{Rb}$ .  $^{93}\text{Kr}$  seems to combine features of both with well-defined peaks exhibited in the lower energy range followed by a rather smooth distribution above 400 keV. The explanation may be due to the relative competition between gamma and neutron emission at levels above the neutron binding energy. Slaughter, Nuh, Shihab-Eldin and Prussin (39) have reported the observation of gamma emission from neutron unbound levels

following the beta decay  $^{87}\text{Br}$ , indicating that photon emission can successfully compete with neutron emission above the neutron binding energy. The effect of such competition on the delayed neutron spectrum following the beta decay of  $^{87}\text{Br}$  is not known due to the lack of detailed knowledge of the delayed neutron spectrum. For the cases of  $^{137}\text{I}$ ,  $^{93}\text{Kr}$  and  $^{93}\text{Rb}$ , no high-energy gamma spectra data are available and so it is not known if gamma and neutron emission compete in the decays of these nuclides or what effect such competition may have on the observed neutron spectra. It is unlikely that the mere fact that competition exists would result in any change of the neutron spectrum since the two emission processes arise independently and obey different selection rules. What would be interesting to ascertain would be the nature of beta-decay to levels nearly degenerate in energy but with considerable differences in properties.

The general features of the fission product delayed neutron spectra observed in this study tend to correlate with their associated group spectra measurements shown earlier in Figure 9. The group 2 spectrum which is composed primarily of  $^{137}\text{I}$  with some possible contribution from  $^{88}\text{Br}$ , bears a strong resemblance to the more highly resolved  $^{137}\text{I}$  spectrum obtained in these measurements as shown in Figure 29. Similarly, the spectra obtained for mass 93 shown in Figure 30 which consists mainly of  $^{93}\text{Kr}$  delayed neutrons appears to

contribute heavily to the group 4 spectrum as indicated by the similarity in the general features of the two. It is clear that detailed spectra measurements of all individual delayed neutron precursors will provide delayed neutron energy characterizations that may be grouped together in any appropriate manner to provide more accurate data for reactor studies.

This study demonstrated that the effectiveness of a  $^3\text{He}$  proportional counter when used as a neutron spectrometer can be greatly enhanced by the use of pulse risetime discrimination techniques. Since the use of risetime discrimination greatly reduces the thermal peak and wall effect pulses and practically eliminates the recoil neutron distribution and gamma-induced pulses, the resultant spectrum does not require extensive unfolding methods to determine the peak energy values. Such is not the case with a  $^3\text{He}$  ionization chamber used as a neutron spectrometer. Even though the energy resolution is better by a factor of two, the inherent microphonic noise characteristics of the detector coupled with its gamma sensitivity make it a less desirable neutron spectrometer than the  $^3\text{He}$  proportional counter, as it is presently configured.

## VI. SUGGESTIONS FOR CONTINUING WORK

The accurate characterization and interpretation of the delayed neutron emission spectra of individual delayed neutron precursors remains one of the least known and understood topics of nuclear physics. The measurement and compilation of detailed spectra for each of the delayed neutron precursors can provide a systematic basis for developing a viable theoretical treatment of the process.

The techniques developed in this work can be applied directly to the study of other delayed neutron precursors as they become available through improvements in the design of fission product sources. Such detailed study of individual precursors is necessary to provide data from which highly accurate compilations of delayed neutron characteristics can be made.

The half-lives of other delayed neutron precursors which can be produced by the present fission product generator design but were not measured in this study due to low signal to background ratio should be studied. Since low levels of delayed neutron activity were observed at masses 87, 90, 91, 94 and 139 during the course of this study, it is likely that accurate half-lives could be determined for the precursors. However, the length of the multiscale runs required might be on the order of days.

One important characteristic of delayed neutron emission is the neutron emission probability of the emitter nuclide. An on-line method of measuring the emission probability of a particular nuclide can be used if the ground-state beta decay branching of the precursor nuclide is known. The decay of the precursor nuclide can be simultaneously time multiscaled using both a gamma and a neutron detector. The gamma detector could be set to monitor a transition that depopulates a level with known beta feeding and both detectors must be calibrated for absolute efficiency. The gamma detector can be used to determine the total decays of the precursor, the neutron counter used to determine the number of decays through the neutron emission channel and hence, the emission probability can be obtained.

The application of risetime discrimination techniques to the  $^3\text{He}$  ionization chamber might produce an extremely good spectrometer provided the microphonic noise sensitivity of the detector could be eliminated. One possibility might be to eliminate the use of the grid portion of the detector by applying bias only to the anode. The detector could then be evaluated and perhaps used as a high resolution proportional counter.

Even without extensive modifications the ionization chamber spectrometer system should be carefully evaluated for

possible improvement since its use was not as successful in this study as was expected from claims by its developer.

## VII. BIBLIOGRAPHY

1. R. Roberts, R. C. Meyer and P. Wang, Phys. Rev., 55, 510 (1939).
2. Ya. B. Zeldovich and Yu. B. Khariton, Zh. Eksp. Teor. Fiz., 10, 477 (1940).
3. S. Yiftah and D. Saphier, "Delayed Fission Neutrons," Panel Proceeding Series, I.A.E.A., Vienna, 1968, p 23.
4. G. R. Keepin, "Progress in Nuclear Energy," Vol. 1, Pergamon Press, London, 1956.
5. L. Tomlinson, United Kingdom Atomic Energy Authority Report No. AERE-R 6596 (1970).
6. H. Gauvin, "Delayed Fission Neutrons," Panel Proceeding Series, I.A.E.A., Vienna, 1968, p 167.
7. H. D. Schussler, H. Ahrens, H. Folger, H. Franz, W. Grimm, G. Herrman, J. V. Kratz and K. L. Kratz, "Second Symposium on Physics and Chemistry of Fission," I.A.E.A., Vienna, 1969, p 591.
8. L. Tomlinson, United Kingdom Atomic Energy Authority Report No. AERE-R 6993 (1972).
9. Arthur H. Jaffey, U.S.A.E.C. Report No. ANL-7747 (1970).
10. Ronald J. Onega, Nucl. Sci. Eng., 43, 345 (1971).
11. L. V. East and G. R. Keepin, "Second Symposium on Physics and Chemistry of Fission," I.A.E.A., Vienna, 1969, p 647.
12. W. L. Talbert, Jr., A. B. Tucker and G. M. Day, Phys. Rev., 177, 1805 (1969).
13. W. L. Talbert, Jr. and J. R. McConnell, Arkiv Fysik, 36, 99 (1967).
14. A. C. Wahl, Private communication to W. L. Talbert, Jr., 1969.
15. P. A. Seeger and R. C. Perisho, U.S.A.E.C. Report No. LA-3751 (1967).

16. G. T. Garvey, W. J. Gerace, R. L. Jaffe, I. Talmi and I. Kelson, Princeton University Report No. PUC-937-331 (1969).
17. J. Wing and P. Fong, Phys. Rev., 136, B923 (1964).
18. N. Bohr and J. A. Wheeler, Phys. Rev., 56, 426 (1939).
19. W. L. Talbert, Jr., Private communication, 1972.
20. S. Amiel in "Nuclear Chemistry," Vol. 2., L. Yaffe, Ed., Academic Press, New York, N.Y., 1968, p 241.
21. P. J. M. Korthoven and F. S. Carlsen, U.S.A.E.C. Report No. IS-1501 (1967)
22. H. Serle, Spectrum Measurements of Radioactive Neutron Sources in the 10 keV-10 MeV Energy Region with Proton-Recoil Proportional Counters, Karlsruhe Nuclear Research Center, External Report No. INR-4170-25, (1970) [transl.: U. S. Department of Commerce Report ORNL-tr-2415, (1970)].
23. R. Bachelor and H. R. McHyder, J. Nucl. Energy, 3, 7 (1956).
24. R. Bachelor and K. Parker, United Kingdom Atomic Energy Authority Report No. AWRE O-78/64 (1964).
25. A. Sayers and M. Coppola, Rev. Sci. Inst., 35, 4 (1964).
26. S. Izumi and Y. Murata, Nuc. Inst. and Meth., 94, 141 (1971).
27. Hsien-Tsan Wang, University of California Report No. UCRL-10770 (1963).
28. S. Greenberger and S. Shalev, Technion-Israel Institute of Technology Report No. TNSD-R/407 (1969).
29. S. Kinbara and T. Kumahara, Nuc. Inst. and Meth., 70, 173 (1969).
30. J. M. Cuttler, S. Greenberger and S. Shalev, Nuc. Inst. and Meth., 75, 309 (1969).
31. John D. Seagrave, U.S.A.E.C. Report No. LAMS-2162, 1969, p 12.
32. R. Sher and J. J. Floyd, Phys. Rev., 102, 242 (1956).

33. S. Shalev, Technion-Israel Institute of Technology Report No. TNSD-R/421 (1971).
34. J. M. Cuttler, S. Shalev and Y. Dagan, Trans. Amer. Nuc. Soc., 12, No. 1, 63 (1969).
35. H. Verheul, Nuclear data sheets for A=87, Nuclear Data, B5, 457 (1971).
36. S. Shalev and G. Rudstam, Phys. Rev. Letters, 28, 687 (1972).
37. G. H. Carlson, W. C. Shick, Jr., W. L. Talbert, Jr., and F. K. Wohn, Nucl. Phys., A125, 267 (1969).
38. G. J. Perlow and A. F. Stehney, Phys. Rev., 113, 1269 (1959).
39. D. R. Slaughter, F. M. Nuh, A. A. Shilab-Eldin and S. G. Prussin, Physics Letters, 38B, 22 (1972).
40. J. H. Norman, W. L. Talbert, Jr., and D. M. Roberts, U.S.A.E.C. Report No. IS-1893 (1968).

## VIII. ACKNOWLEDGEMENTS

The author would first like to thank Dr. W. H. McCorkle who nearly 16 years ago served as the initial source of inspiration that resulted in the author's pursuit of a graduate education. The author's close association with this man during most of those years was an educational experience that few have been privileged to enjoy.

It is unlikely that the completion of this project would have been possible without the liaison efforts of Dr. Donald M. Roberts. His forebearance and patience as the major professor of a part-time student is gratefully acknowledged.

Dr. Fred K. Wohn, as a member of the TRISTAN team, provided much help and assistance in all stages of the project. His help during the precursor identification work and neutron spectrometer calibration measurements was especially appreciated.

To Mr. Harold Skank and Mr. Gary Sleege of the Instrumentation group, the author expresses sincere thanks for their successful efforts in keeping the various pieces of electronics functioning properly.

The author is deeply indebted to Mr. John R. McConnell for the successful completion of this project. His untiring efforts and boundless enthusiasm during data collection and the frequent system modifications necessary for this study

made the task possible. His help was essential and the selflessness with which he gave it will not be forgotten.

Dr. W. L. Talbert, Jr. who as leader of the TRISTAN group made the system available so that this study could be undertaken deserves a special thanks. My appreciation for his advice and guidance during all phases of the work can not be adequately expressed.

Finally, to my wife, Ann, whose patient indulgence has made the burdens lighter, I dedicate this thesis.

## IX. APPENDIX A: ACTIVITY SEPARATION TECHNIQUES USING A MOVING TAPE COLLECTOR

### A. Introduction

There are several modes of operation of a moving tape collector (MTC) connected to an on-line mass separator that are useful in separating activities in a decay chain. The program ISOBAR (40) analyzes two modes of operation, continuous tape motion with the detector at the deposit point and discontinuous tape motion with the detector at either the deposit point or at a downstream point. The second mode is referred to as "Daughter Analysis" (DA).

There are two other methods of operation which are used extensively for data collection: equilibrium counting at the deposit point and the "High Duty Factor" (HDF) mode at a downstream point.

This appendix defines the data collection modes and describes the modifications made to the original ISOBAR program (40) to calculate the data collection efficiency for each mode of operation.

### B. Definition of Data Cycles

With regard to data collection using a MTC, there are two basic modes of operation: collecting at the beam deposit

point (detector-1), and collecting at a downstream point (detector-2).

At detector-1 there are three useful types of data cycle; continuous tape motion ('CONT'), discontinuous tape motion ('DISC'), and equilibrium counting ('EQBR'). At detector-2 the two most useful data cycles are daughter analysis ('DA') and high duty factor ('HDF'), although under certain conditions (for example, when conserving tape is of paramount interest) it may be advantageous to use the DA mode at detector-1.

The definition of a data cycle (DC) involves the relationship of four time parameters; the beam deposit time, T, the delay time between beam deposit and data collection, TAUD, the data collection time, TAUC, and the time required to move the tape, TM. (During the continuous mode of tape operation all four times are set by the actual tape speed and the mechanical design of the tape collector.) The HDF mode of operation requires that four digital switches, T1, T2, T3, and T4, on the daughter analysis control unit be set to yield the desired values of T, TAUD, TAUC, and TM, according to the relations below.

$$T = T_1 + T_2$$

$$TAUD = T_1 + T_3 + T_4$$

$$TAUC = T_2 + T_3$$

$$TM = T_4$$

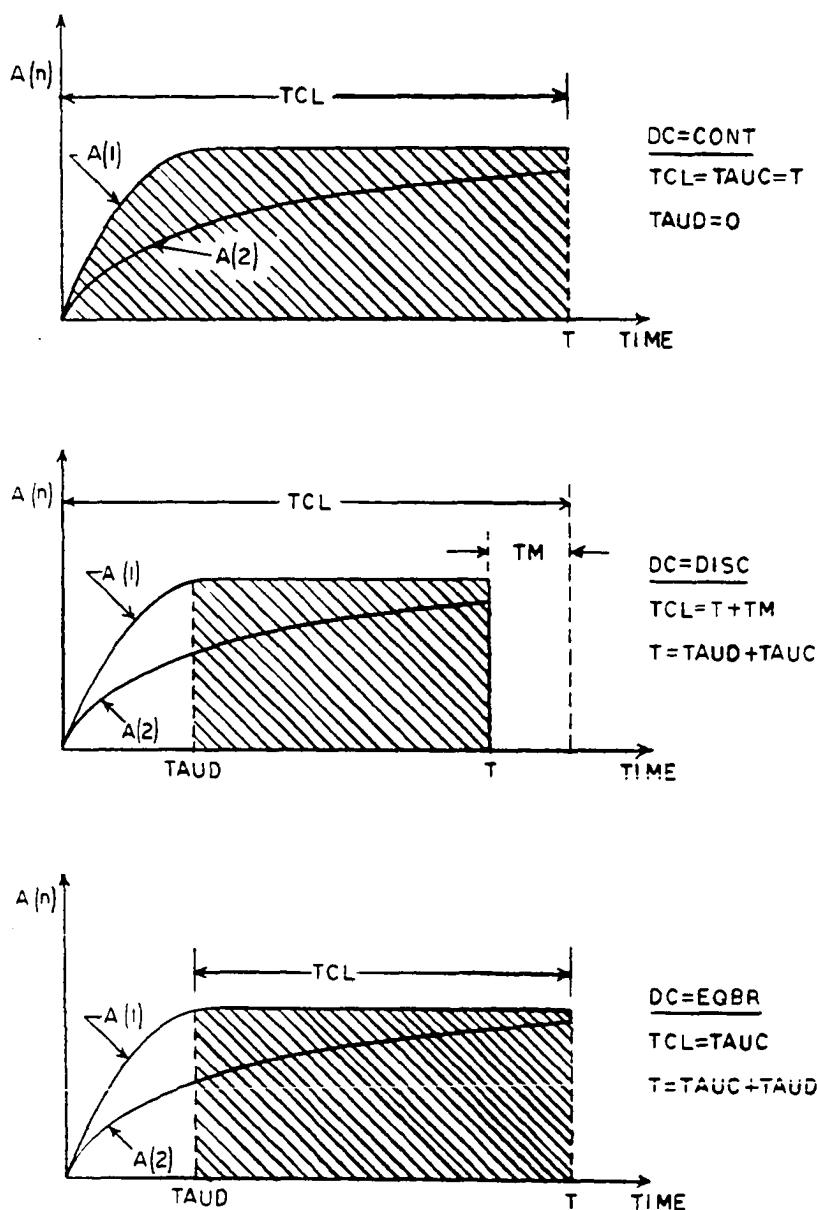


Figure 32. MTC data cycles at detector-1

The data cycles used at detector-1 are shown in Figure 32 and those used at detector-2 are shown in Figure 33. Both figures show the activity buildup of a hypothetical two-member decay chain. Identified for each cycle is the total cycle length (TCL), the relationships between the various time settings, and the data collection period indicated by the cross-hatched area. It should be noted that the data cycles at detector-1 involve data collection during activity buildup and data cycles at detector-2 involve data collection during the activity decay period. A brief description of each data cycle follows:

DC='CONT'

This data cycle is used to observe the parent member of a decay chain using continuous tape motion with the detector at the activity deposit point. The beam deposit and data collection times are determined by tape speed.

The ISOBAR inputs required to analyze this mode of operation are the decay chain observed, the data cycle mode, and the tape speed.

DC='DISC'

This data cycle uses discontinuous tape motion to observe the parent member or first few members of a decay chain at the activity deposit point. For this case a delay

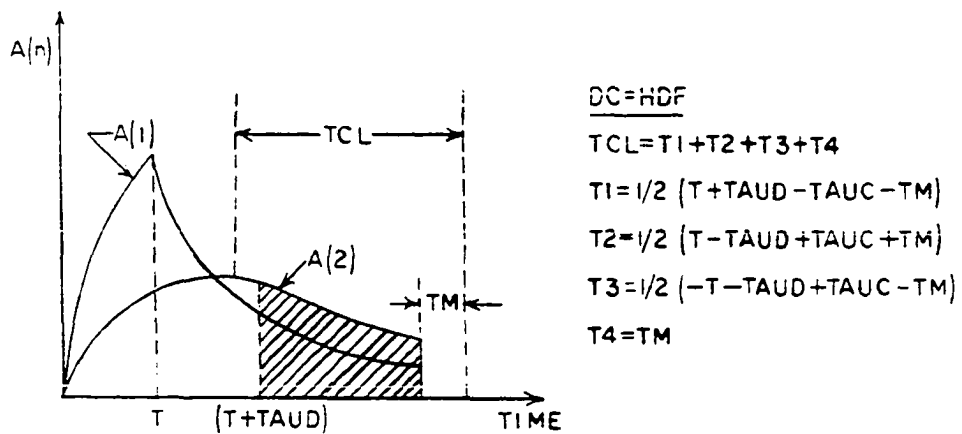
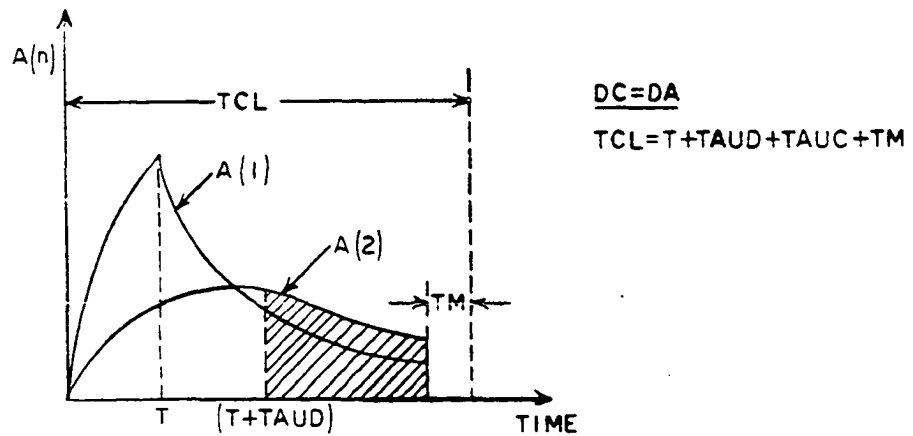


Figure 33. MTC data cycles at detector-2

period may be used after beam deposit is initiated prior to the beginning of data collection. Following data collection the tape is moved and the cycle may be repeated.

The ISOBAR inputs required are the decay chain observed, the data cycle mode, and the values of T, TAUD, and TM.

DC='EQBR'

This data cycle uses a stationary tape to observe the total decay chain in equilibrium at the activity deposit point. A delay period may be used at the start of the cycle to allow the longest half-life of interest in the decay chain to reach equilibrium before data collection is begun.

The ISOBAR inputs required are the decay chain observed, the data cycle mode, and the values of T and TAUC. A delay is inserted at the start of the cycle for  $T > TAUC$ .

DC='DA'

This data cycle uses discontinuous tape motion to observe a daughter activity. Normally, the beam is deposited for a time, T, and the tape is then moved to a detector located downstream for data collection. However, this mode may be used to observe daughter activities at the activity deposit point if the tape is moved at the end of the data cycle as shown in the figure.

The ISOBAR inputs required are the decay chain observed, the data cycle mode, and the values of T, TAUD, TAUC, and TM.

DC='HDF'

This data cycle requires activity collection at the beam deposit point and data collection at a downstream location. The advantage of this data cycle is that a second sample may be collected at the activity deposit point while data is being collected at the downstream detector location. The various time relationships in the cycle are determined by the settings of T1, T2, T3, and T4 on the daughter analysis control (DAC) unit. Since the values of the DAC settings can not be negative the following relationships must be satisfied for this mode of operation.

$$T1 \geq 0 ; T + TAUD \geq TAUC + TM$$

$$T2 \geq 0 ; T + TAUC + TM \geq TAUD$$

$$T3 \geq 0 ; TAUD + TAUC \geq T + TM$$

$$T4 \geq 0 ; TM \geq 0$$

The ISOBAR inputs required are the decay chain observed, the data cycle mode, and the values of T, TAUD, TAUC, and TM.

### C. Summary of ISOBAR Modifications

The original version of ISOBAR, as described in reference (40), calculated percent of the saturated activity, activity ratio, and integrated activity ratio of each member of a fission product decay chain given the collect, delay, and count times. The program was used to obtain the best combination of time parameters to yield the highest integrated activity ratio while maintaining an adequate count rate as indicated by the fraction of saturated activity.

Another useful indicator of the best combination of collect, delay, and count times is the calculated collection efficiency over the data cycle time. The collection efficiency is defined as the ratio of the calculated integrated activity ratio (for the collect, delay, count, and tape transport time settings to be used) to the maximum counting efficiency condition which is taken to be equilibrium counting. The collection efficiency or true data acquisition rate over the data cycle may then be balanced against the desired activity separation of each member in the decay chain as a test of the suitability of the selected time parameters. In addition, if the time parameters are fixed by the experimental setup or by the fixed tape speed in the case of continuous tape motion, the calculated collection efficiency can be multiplied by the integrated activity ratio and the observed decay chain equilibrium count rate to yield the

total number of counts of each decay chain member that may be expected over the data cycle.

The two basic counting conditions for a MTC system are counting at detector-1 and counting at detector-2. The equations developed for the original version of ISOBAR apply to counting at detector-2 and require no modification. However, counting at detector-1 requires some additional consideration since data collection occurs simultaneously with beam deposit. For the development of proper integrated activity equations it is sufficient to integrate the general activity equation between the proper limits.

The general equation for the activity buildup and decay of a member of a beta-decay chain is given by equation 12 of reference (40). Since in the referenced equation the delay time is the time after beam deposit ends for counting at detector-1, with the delay time set equal to zero the resulting equation describes the activity buildup as shown in the examples in Figure 32.

To obtain the integrated activity for the cases shown in Figure 32 it is necessary only to integrate the activity equation between the desired limits for the particular case being considered. Since the maximum possible number of counts obtainable over the total data cycle is proportional to the activity deposition rate multiplied by the time of the total cycle length, the collection efficiency can be readily

calculated.

The ISOBAR program was therefore modified to include the collection efficiency calculation for each member of the decay chain under consideration. The input data required for the modified program are sequentially; a) number of the mass chain of interest, b) detector position (1 or 2), c) type of data cycle being used, d) time parameters as required by the program.

#### D. ISOBAR Calculation for Mass 93

An example of the use of ISOBAR was the determination of activity separation in the mass 93 decay chain. Since both Kr and Rb are delayed neutron precursors it was necessary to operate the MTC in such a manner that both could be observed in equilibrium and each could be observed enhanced with respect to the other.

Table 8 shows the results of the calculations using ISOBAR. The first entry gives the true equilibrium condition for Kr and Rb. The time entries are in seconds and both activities are saturated. The calculated count rate for both Kr and Rb would be identical were it not for differences in the emission probability for each associated precursor. As a result, Kr, which has a larger neutron emission probability, is enhanced even under equilibrium counting conditions.

Table 8. ISOBAR calculations for mass 93

Type of Activity	Type of Data Cycle	T	TAUD	TAUC	TM	Chain Member	Calc. Count Rate*
Kr & Rb eqbr.	'EQBR'	82800		77400	0	Kr Rb	6.3 3.7
Kr & Rb eqbr.	'DISC'	117	0	117	3	Kr Rb	6.2 3.2
Kr enhanced	'DISC'	6	0	6	1	Kr Rb	5.3 0.2
Rb enhanced	'DA'	15	4	17	2	Kr Rb	0.004 1.2

\* Normalized to an observed equilibrium count rate of 10 counts per second, and modified to include the differences in neutron emission probability.

One problem with equilibrium counting using long collection times is the large gamma background buildup due to longer lived members of the decay chain which are not neutron precursors. The second entry in the table shows how such buildup can be eliminated. In this case the beam was deposited and data were collected only as long as required to have the Kr and Rb activities near equilibrium and then the tape was moved to remove the longer-lived components. It is obvious from the calculated count rate that counting under such near-equilibrium conditions has only a small effect on the expected count rate. The Kr activity enhancement over that of Rb for the near-equilibrium case is about a factor of 2.

The third entry shows the effect of further enhancing the contribution of Kr by discontinuous tape movement to move the Rb daughter component away from the detector. From the calculated count rate it can be seen that the Kr activity enhancement over that of Rb was increased to a factor of about 25 at the cost of about a factor of two in total count rate.

The fourth entry shows how the Rb daughter activity can be enhanced by operating the tape in the DA mode. The times selected yield a Rb-to-Kr activity enhancement of about 300. However, the total count rate for such conditions is reduced by about a factor of 8 below the equilibrium counting condition.

It should be noted that the calculated count rate for each chain member in Table 8 is just the integrated activity ratio multiplied by the collection efficiency and the result normalized to the observed equilibrium count rate for the decay chain. For the case of delayed neutron emission shown in the table, the count rate calculation must also be modified to include the neutron emission probability for each precursor in the decay chain.

## X. APPENDIX E: EXPERIMENTAL EQUIPMENT USED

This section lists the details of the experimental equipment shown in schematic form in Figures 8, 14, and 23. The equipment is identified and the important instrument settings are specified in order to facilitate experimental setup and checkout.

Equipment identification is by manufacturer, model number, and Ames Laboratory property number (P/N) to provide positive identification.

### A. Half-life Measurements

Long counter: Specially designed and locally fabricated detector containing five Amperex type 102 BF-3 chambers and five ALRR type 1109 preamplifiers.

Detector bias: Hamner-N-4035, P/N-268; polarity-positive, high voltage setting-1750 coarse/0100 fine.

Preamp power supply: CI-1400, P/N-13955.

Test pulser: Geos-2010, P/N-16342; settings as required.

Summing amplifier: ALRR-1122, P/N-16503; individual channel gain adjusted to yield a 4 volt peak signal for each detector at the main amplifier output.

Main amplifier: CI-1410, P/N-14469; input-negative and terminated, course gain-54, fine gain-8, first differentiation-2, second differentiation-2, integration-2, output-prompt bipolar to multichannel analyzer and prompt

unipolar to single channel analyzer.

Single channel analyzer: CI-1430, P/N-13809; baseline-0230, window-0640, scaler output-to timer/scaler.

Timer/scaler: ALRR-002/003, P/N-15733/15738.

Multichannel analyzer ADC: Geos-8050, P/N-16968; lower level-0160, upper level-1000, range-8192, compression-4/1, conversion-4096/8volts.

#### B. $^3\text{He}$ Proportional Counter

$^3\text{He}$  detector: Texas Nuclear-9341, P/N-13784.

Charge sensitive preamplifier: Ortec-120-3F, P/N-17072.

Detector bias: Honeywell-6K20, P/N-11380; polarity-positive, high voltage setting-2100 volts.

Preamp power supply: CI-1400, P/N-14076.

Precision pulser: Berkeley Tail-Pulse Generator-RP 1, P/N-13253; settings-as required.

Risetime amplifier: MT-501, P/N-16356; gain- $2 \times 1 \times 0643$ , clip 1-0.8, clip 2-3.2, integration-out, 93 ohm, normal-divide by 1, both, internal, input-Es, output-clip 2.

Pulse shape analyzer: Ortec-458, P/N-18114; range- $0.2 \times 10$ , threshold- $0150 \times 10$  volts, upper level-1000, lower level-0000.

Biased amplifier: CI-1467, P/N-18128; bias-0313, gain- $2 \times 0797$ , range-10, positive, coincidence, restorer-hi.

Risetime ADC: Geos-8050, P/N-16907; input-pulse,

termination-out, restorer-log/out/12.8, coincidence-coinc/gate/out, conversion-4096/8 volts, compression-1/1, range-4096.

Pulse height amplifier: TC-203BLR, P/N-17802; gain-20x0938, time constant-4 microsecond, input-direct, BLR-out, rate-low, delayed output-direct, output-DC delayed.

Biased amplifier: CI-1467, P/N-18293; bias-0, gain-2x.5, range-10, positive, coincidence, restorer-hi.

Pulse height ADC: Geos-8050, P/N-16963; input-pulse, termination-out, restorer-log/out/12.8, coincidence-coinc/gate/out, conversion-4096/8 volts, compression-1/1, range-4096.

ADC coincidence-gate generator: Ortec-416, P/N-13778; range-1.0 to 11, delay-0516, width-3.8 microseconds, amplitude-4 volts.

Data strobe generator: Ortec-416, P/N-14067; range-0.1 to 1.1, delay-0288, width-3.8 microseconds, amplitude-4 volts.

Timer/scaler: ALRR-002/003, PN-15733/15738.

Two-parameter display: Geos-4000, P/N-16968; two-parameter control programmed for a 256x16 storage and display, pulse height ADC-compressed to 256 channels, risetime ADC-compressed to 16 channels.

### C. $^3\text{He}$ Ionization Chamber

$^3\text{He}$  detector: Technion-IC45, P/N-18314.

Anode/guard bias: Fluke-408B, P/N-16887; polarity-positive, high voltage setting-5000 volts, noise filter-attached to high voltage output.

Grid bias: Fluke-412B, P/N-14711; polarity-positive, high voltage setting-1200 volts, noise filter-attached to high voltage output.

Preamplifier: Ortec-120-3F, P/N-17072.

Preamp power supply: CI-1400, P/N-14076.

Precision pulse generator: Berkley Tail Pulse Generator-RP 1, P/N-13253; rate-18 cps, normalize-0476, amplitude-0266, risetime-5 microseconds, fall time-100 microseconds, attenuation-x10.

Main amplifier: TC-203 BLR, P/N-17802; gain- $100 \times 1021.5$ , time constant-8 microseconds, BLR-in, rate-low, input-direct, output-unipolar/DC.

Multichannel analyzer ADC: Geos-8050, P/N-16963; input-pulse, term-out, lower level-0020, upper level-1000, restorer-passive, pileup reject-on, conversion-4096/8 volts, compression-4/1, range-4096.

Zero stabilizer: Geos-2000, P/N-17270; peak select-608, mode-normal, window width-15, analog correction-1/2.

Gain stabilizer: Geos-2000, P/N-17269; peak select-3000, mode-normal, window width-15, analog correction-1/2.

Timer/scaler: ALRR-002/003, P/N-15733/15738.